Atmos. Chem. Phys. Discuss., 5, 2989–3046, 2005
www.atmos-chem-phys.org/acpd/5/2989/
SRef-ID: 1680-7375/acpd/2005-5-2989
European Geosciences Union

Atmospheric Chemistry and Physics Discussions

Retrieving the vertical distribution of stratospheric OClO from Odin/OSIRIS limb-scattered sunlight measurements

P. Krecl[1], **C. S. Haley**[2], **J. Stegman**[1], **S. M. Brohede**[3], **and G. Berthet**[4,*]

[1]Department of Meteorology, Stockholm University, Stockholm, Sweden
[2]Centre for Research in Earth and Space Science, York University, Toronto, Canada
[3]Department of Radio and Space Science, Chalmers University of Technology, Göteborg, Sweden
[4]Service d'Aéronomie, Institut Pierre-Simon Laplace, Paris, France
[*]now at: Department of Applied Mathematics and Theoretical Physics, University of Cambridge, Cambridge, UK

Received: 28 February 2005 – Accepted: 29 March 2005 – Published: 13 May 2005

Correspondence to: P. Krecl (patricia@misu.su.se)

Abstract

The first vertical profiles of stratospheric OClO retrieved from Odin/OSIRIS limb-scattered sunlight radiances are presented. The retrieval method is based on a two-step approach, using differential optical absorption spectroscopy combined with the maximum a posteriori estimator. The details of the spectral window selection, spectral corrections and inversion technique are discussed. The results show that OClO can be detected inside the South polar vortex region between about 12 and 20 km altitude with a 2–5 km height resolution and an estimated retrieval error better than 60% at the peak. OClO concentrations are consistent with chemical transport model simulations and show the expected relation to the atmospheric conditions in the lower stratosphere in the austral spring 2002. This unique data set of OClO profiles is very promising to study the stratospheric chlorine activation in both polar regions.

1. Introduction

Since the dramatic ozone destruction over Antarctica was discovered by Farman et al. in 1985, laboratory and model studies in combination with stratospheric observations have improved the scientific understanding of the complex and interactive processes behind this annual depletion (review of historical research in Solomon, 1999). Moreover, these studies have revealed that a less severe stratospheric ozone loss occurs over the Arctic region during springtime (WMO, 2003). Stratospheric ozone is destroyed in the polar regions by several catalytic cycles involving reactive halogen species, primarily chlorine and bromine. Polar stratospheric clouds (PSCs), which are formed during the cold and dark winter, play a crucial role in the so-called chlorine activation. This activation refers to the conversion of chlorine reservoir gases (including HCl and $ClONO_2$) into the more reactive forms (ClO and ClOOCl) by heterogeneous reactions occurring on the surface of the PSC particles. One of the consequences of the chlorine activation is the formation of chlorine dioxide (OClO) mainly by the reaction

ACPD

5, 2989–3046, 2005

$$ClO + BrO \rightarrow OClO + Br, \quad (R1)$$

that occurs in the lower stratosphere. OClO is rapidly photolyzed producing ClO and O,

$$OClO + h\nu \rightarrow ClO + O, \quad (R2)$$

leading to a null cycle when atomic oxygen combines with molecular oxygen to reform ozone. Even though OClO is not directly involved in the ozone destruction, its concentration is a quantitative indicator of the degree of chlorine activation at solar zenith angles (SZA) lower than 92° (Sessler et al., 1995).

The presence of OClO in the atmosphere was first detected at McMurdo Station (Antarctica) by Solomon et al. (1987) during the austral spring in 1986. Since then, total column densities of OClO have been derived from ground-based, airborne, and satellite measurements in the Arctic and Antarctic regions (e.g., Sanders et al., 1989; Schiller et al., 1990; Perner et al., 1991; Brandtjen et al., 1994; Wagner et al., 2001). Though measurements of OClO total column amounts are important, the OClO vertical distribution is required to improve the model computations of the ozone destruction due to the BrO/ClO reaction. It is also important to increase the confidence in the assumed relation between the stratospheric levels of BrO and OClO in the model calculations. Despite the relevance of these profiles, OClO vertical concentrations have been only measured in a few balloon campaigns in northern Scandinavia (e.g., Pommereau and Piquard, 1994; Renard et al., 1997; Payan et al., 1999; Rivière et al., 2003).

The need for global coverage and high vertical resolution of atmospheric information led to the development of the atmospheric limb-scattering technique. In this complex viewing geometry, sunlight scattered from the Earth's limb is continuously measured on the sunlit atmosphere at different tangent heights. Some recently launched satellite instruments measure limb radiances with the objective of retrieving the vertical distribution of trace gases, including OClO. The Optical Spectrograph and InfraRed Imager System (OSIRIS) onboard the Odin satellite (Llewellyn et al., 2004) and the Scanning

ACPD
5, 2989–3046, 2005

Imaging Absorption spectroMeter for Atmospheric CHartographY (SCIAMACHY) on the ENVISAT spacecraft (Bovensmann et al., 1999) were specially designed to measure limb-scattered sunlight radiances with a near-global coverage and high vertical resolution (1–3 km). Two other instruments, the Global Ozone Monitoring by Occultation of Stars (GOMOS) also onboard ENVISAT (Bertaux et al., 1991) and the Stratospheric Aerosol and Gas Experiment III (SAGE III) on the Meteor-3M platform (McCormick et al., 1991), are primarily occultation instruments, but also have a limb-scatter measurement capability.

This paper reports the first OClO number density profiles retrieved from OSIRIS limb-scattered radiances using differential optical absorption spectroscopy (DOAS) (Platt, 1994) combined with an optimal estimation (OE) method, more specifically the maximum a posteriori (MAP) estimator (Rodgers, 2000). After a summary of OSIRIS and Odin characteristics is given, the retrieval algorithm is described together with some sensitivity studies of the calculated OClO effective column densities (ECD). OSIRIS OClO profiles are then compared with simulations from a chemical transport model and some balloon measurements performed in the past. Results for high chlorine activation conditions in the austral spring 2002 are presented together with an outlook of the future work to be done.

2. OSIRIS instrument

The Odin satellite has a joint aeronomy and astronomy mission (Murtagh et al., 2002), sharing the main instrument which is an advanced Submillimetre and Millimetre Radiometer (SMR) (Frisk et al., 2003). For the aeronomy mission, the payload is complemented by another passive remote sensing instrument, OSIRIS (Llewellyn et al., 2004). Odin was launched in February 2001 into a 600 km circular Sun-synchronous near terminator orbit with the ascending node at 18:00 local solar time (LST). The coaligned instruments scan the terrestrial limb between 7 and 70 km tangent height in the stratospheric mode or between 7 and 110 km for the stratospheric-mesospheric

mode at a rate of 0.75 km s^{-1} through nodding of the spacecraft. Odin completes about 15 orbits per day and, when operated in the stratospheric mode, approximately 65 scans are carried out per orbit. The inclination of Odin's orbit is 97.8°, limiting the latitudinal coverage to between 82.2° N and 82.2° S when viewing in the orbit plane. An off-plane mode is occasionally used to provide better global coverage, for example during the ozone 'hole' period. OSIRIS consists of two optically independent components: the Optical Spectrograph (OS) and the Infrared Imager (IRI). The spectrograph uses a charged-coupled device that provides a spectral coverage from 280 to 800 nm with a resolution (FWHM) of approximately 1 nm. The instantaneous field of view is 1 km in the vertical and 40 km in the horizontal at the tangent point. This study is focused on the OS, since chlorine dioxide absorbs in the UV-visible region. Table 1 summarizes the mission, spectral intervals (frequency or wavelength) and target species for the instruments onboard Odin.

3. Methodology

The two-step method developed by Haley et al. (2004) is used to derive OClO vertical number density profiles from OS limb-scattered sunlight measurements in the near-UV and violet regions of the solar spectrum. The first step is the spectral analysis of the OS measurements to calculate the OClO ECD profiles by applying the DOAS technique. The second step is the inversion of these ECD profiles to obtain the number density profiles using a non-linear iterative version of the MAP estimator coupled with the LIMBTRAN (Griffioen and Oikarinen, 2000) radiative transfer model. Figure 1 shows a schematic description of the retrieval algorithm.

3.1. Spectral analysis

In the late seventies, DOAS was introduced as a method to detect atmospheric trace-gas concentrations from measurements in the UV and visible spectral regions (e.g.,

ACPD
5, 2989–3046, 2005

Noxon, 1975; Noxon et al., 1979, and Platt et al., 1979). This technique uses narrow molecular absorption bands of trace species, which are molecule-specific, to deduce their absorption strength. A detailed description of DOAS applied to scattered sunlight limb radiances follows.

Absorption spectroscopic techniques employ the Beer-Lambert-Bouguer Law to determine the concentrations of gas species. This law describes the pure absorption of electromagnetic radiation by a single species in a homogeneous medium at a specific wavelength, and has to be modified when applied to limb-scattered sunlight measurements. It is necessary to add the contribution of Rayleigh and Mie scattering, and to consider multiple absorbers over a spectral region. Thus, the optical depth τ at tangent height h_t and wavelength λ can be expressed as

$$\tau(\lambda, h_t) = \ln\left[\frac{I_o(\lambda)}{I(\lambda, h_t)}\right] = \sum_i \sigma_i(\lambda) c_i(h_t) + \tau_R(\lambda, h_t) + \tau_M(\lambda, h_t), \quad (1)$$

where $I(\lambda, h_t)$ is the measured intensity, $I_o(\lambda)$ is the unattenuated reference intensity, $\sigma_i(\lambda)$ is the wavelength dependent absorption cross section of the ith species, $c_i(h_t)$ is the effective column density of the ith species as measured in the direction of the line of sight (LOS), $\tau_R(\lambda, h_t)$ is the Rayleigh optical depth, and $\tau_M(\lambda, h_t)$ is the Mie optical depth. Note that in the limb viewing geometry, I_o represents a scattered solar spectrum free from molecular absorption and Rayleigh and Mie extinctions. Since such a spectrum is not available from OS measurements, a limb-scattered spectrum from a high tangent height within the same scan is used. This reference is expected to contain little trace gas absorption, thus maximizing the differential absorption features while minimizing the interference with the solar Fraunhofer lines. The average of limb-scattered spectra between 40 and 70 km from each scan is used as the reference to reduce noise.

The basic principle of DOAS is to calculate the so-called differential absorption, that is the rapidly varying part of the total absorption. Hence, the absorption cross sections

ACPD
5, 2989–3046, 2005

are split into two components:

$$\sigma_i(\lambda) = \sigma_i^s(\lambda) + \sigma_i'(\lambda), \quad (2)$$

where $\sigma_i^s(\lambda)$ represents broad spectral features and the differential cross sections, $\sigma_i'(\lambda)$, show narrow spectral features containing the 'fingerprints' of the absorbers. Introducing Eq (2) into Eq. (1), and separating the rapidly and slowly varying components leads to

$$\tau(\lambda, h_t) = \underbrace{\sum_i \sigma_i'(\lambda) c_i(h_t)}_{rapid, \tau'} + \underbrace{\sum_i \sigma_i^s(\lambda) c_i(h_t) + \tau_R(\lambda, h_t) + \tau_M(\lambda, h_t)}_{slow, \tau^s}, \quad (3)$$

where the first term of the right-hand side is the differential optical depth (DOD), and the other three terms represent the slowly varying components of the optical depth τ^s. Considering only the differential component of Eq. (3), the differential optical depth τ' is defined as

$$\tau'(\lambda, h_t) = \sum_i \sigma_i'(\lambda) c_i(h_t). \quad (4)$$

The observed DOD τ'_{obs} can then be modelled with Eq. (4), i.e.

$$\tau'_{obs}(\lambda, h_t) \approx \sum \sigma_i'(\lambda) c_i(h_t) + E_{\tau'_{obs}}(\lambda, h_t), \quad (5)$$

where $E_{\tau'_{obs}}(\lambda, h_t)$ is the error in the observed DOD resulting from the measurement error (noise) of OS. Employing the error propagation formula, the standard deviation of this error, $\varepsilon_{\tau'_{obs}}(\lambda, h_t)$, is approximated by

$$\varepsilon_{\tau'_{obs}}(\lambda, h_t) = \sqrt{\left[\frac{\varepsilon_{I_o}(\lambda)}{I_o(\lambda)}\right]^2 + \left[\frac{\varepsilon_I(\lambda, h_t)}{I(\lambda, h_t)}\right]^2}, \quad (6)$$

where $\varepsilon_{I_o}(\lambda)$ is the estimated error of the reference spectrum and $\varepsilon_I(\lambda, h_t)$ is the estimated error in the spectrum $I(\lambda, h_t)$.

The effective column densities of the i absorbers at each tangent height can be derived using a least squares (LSQ) fit of Eq. (5) with respect to c, i.e. by fitting the differential cross sections of the absorbers to the observed DOD. A residual analysis is carried out to assess the adequacy of the fit to the measured values. The fitting residual r is defined as the difference between the differential optical depth of the observed and modelled spectra at each tangent height h_t and wavelength λ:

$$r(\lambda, h_t) = \tau'_{obs}(\lambda, h_t) - \sum_i \sigma'_i(\lambda) c_i(h_t). \quad (7)$$

The residual gives a measure of the overall quality of the fit and would consist of only random noise for a perfect model and an ideal measurement. The root mean square (RMS) of the residuals at the tangent height h_t is determined by

$$r_{\mathrm{RMS}}(h_t) = \sqrt{\frac{\sum_{j=1}^{\eta} r(\lambda_j, h_t)^2}{\eta}}, \quad (8)$$

where η is the number of pixels in the fitting region. A chi-squared test is also performed to determine if the fit to the DOD is consistent with the measured DOD within the estimated error of the measurements. The DOAS reduced chi-squared statistic χ^2_{doas} is calculated as

$$\chi^2_{doas}(h_t) = \frac{\sum_{j=1}^{\eta} \left[\frac{r(\lambda_j, h_t)}{\varepsilon_{\tau'_{obs}}(\lambda_j, h_t)} \right]^2}{d}, \quad (9)$$

where d is the number of degrees of freedom (i.e., the number of pixels in the spectral window minus the number of parameters used in the fit). If the reduced chi-squared

ACPD
5, 2989–3046, 2005

values are much larger than one, the observed DOD does not fit the calculated DOD within the measurement errors. Fits with χ^2_{doas}>4 are excluded from the further analysis.

3.2. Selection of the fitting interval

The spectral absorption structure of OClO, shown in Fig. 2, suggests that the differential absorption spectroscopy is an attractive way of detecting this gas in the near-UV and visible regions. Solomon et al. (1987) first retrieved OClO column abundances in the wavelength range of 403–428 nm using a spectrograph covering the region from 400 to 453 nm. Spectroscopic measurements of OClO have also been performed in the near-UV region by other authors (e.g., Schiller et al., 1990; Perner et al., 1991, 1994; Brandtjen et al., 1994; Van Roozendael et al., 1995; Wagner et al., 2001), with the window 363–391 nm being the most frequently employed.

In this study, the selection of the OClO fitting window is restricted to the 355–427 nm wavelength interval. Wavelengths longer than 355 nm are chosen to avoid the imperfect removal of ozone features due to the temperature dependence of its cross sections in the Huggins bands and the non-linearity problems due to large optical depths. Because of a strong N_2^+ auroral emission at 427.8 nm and the weak cross sections of OClO at longer wavelengths, wavelengths have to be shorter than 427 nm. In this study, three spectral regions were investigated as possible fitting windows to retrieve OClO ECD: 363–391 nm, 403–427 nm, and 363–427 nm. Measurements in the 390.9–398.4 nm range are not included in the spectral fit due to the presence of a pair of deep Fraunhofer lines (~393 and ~397 nm) and a strong N_2^+ auroral emission at 391.4 nm. As seen in Fig. 2, other trace gases (i.e., O_3, NO_2, O_4 and BrO) absorb in the UV-visible region. Thus, their absorption cross sections are included along with OClO in the fit. Table 2 displays the number of pixels η of each window, excluded wavelength bands and interfering species in the different windows.

Figure 3 shows OClO ECD profiles, reduced chi squared and residual RMS values retrieved from OS spectra (scan 8567046, measured on 19 September 2002) in the

three spectral regions. The wavelength interval 403–427 nm presents larger OClO ECD compared with the others at almost all the tangent heights. The mean residual RMS values are 1.8×10^{-3}, 1.0×10^{-3}, and 1.6×10^{-3} in the 363–391, 403–427, and 363–427 nm regions respectively with generally larger residual RMS values at lower tangent heights. χ^2_{doas} values in the 403–427 nm window are smaller or at most comparable with the values obtained in the other windows at all tangent heights, ranging between 1 and 2. The estimated accuracy of the OClO ECD at the peak is 12%, 14% and 19% in the 363–391, 403–427, and 363–427 nm windows, respectively.

Since a good reduced chi squared and small residual RMS may not mean necessarily that the fit and/or the fitting function are good, a visual examination of the residuals is performed to identify remaining patterns or systematic structures. Figure 4 presents the fitting residual values of the same scan shown in Fig. 3 at a tangent height of 16.8 km. Although the residuals in the 403–427 nm region show some systematic structures, their values are small compared with the residuals of the other windows. These findings are confirmed with the results obtained when processing other OS spectra measured on 19–20 September 2002 inside the polar vortex area. A significant cross correlation between OClO and BrO absorption cross sections for wavelengths shorter than 380 nm could, to some extent, explain the larger residual structures found in the 363–391 and 363–427 nm intervals and the large difference in ECD.

Negative OClO ECD were frequently found at latitudes outside the polar vortex area at all tangent heights and at high tangent heights (above 25 km) within the vortex for spectra measured on 19–20 September 2002. This is consistent with the negative OClO abundances observed by other authors (e.g., Solomon et al., 1987; Pommereau and Piquard, 1994) outside the chlorine activation area, and is due to the low OClO concentrations. The frequency of occurrence and the magnitude of these negative ECD values are smaller in the range 403–427 nm compared to the values calculated in the other windows. A possible explanation could be the smaller residual structures observed in this spectral window, indicating a better fit.

Based on these results, the window 403–427 nm has been chosen to retrieve OClO

in this study.

3.3. Spectral corrections

Systematic structures in the residual spectra can be caused by the Ring effect, I_o effect, polarization sensitivity of the instrument, effect of instrument resolution and sampling, wavelength shifts, as well as temperature dependence of the absorption cross sections. In this section, the sensitivity of the derived OClO effective columns to these issues is analyzed by applying different spectral corrections to the OS spectra and absorption cross sections. The spectra were chosen from 122 scans, measured on 19–20 September 2002 inside the chlorine activation area, at tangent heights between 10 and 30 km. This study was carried out in a sequence of several steps as follows:

i The variables OClO ECD, relative ECD error (i.e., the ECD error divided by its corresponding ECD), reduced chi squared, and residual RMS are derived when no correction is used in the retrieval process (run 1).

ii The same variables are calculated when the first spectral correction is taken into account (run 2).

iii For each variable, the results of run 1 are subtracted from the results of run 2.

iv These differences are then classified as positive or negative increments. Differences larger than 100% or smaller than −100% represent only a few percent of the total number of measurements and were discarded from this analysis.

v The relative frequencies (i.e., the number of measurements following this condition divided by the total number of measurements) of the positive and negative differences are calculated for each variable.

vi The mean values of the positive and negative increments are computed separately for OClO ECD, relative ECD error, reduced chi squared, and residual RMS.

ACPD
5, 2989–3046, 2005

vii After analyzing the results obtained in steps v) and vi), it is decided if the spectral correction is included or not in the subsequent runs.

The above procedure is employed to investigate the sensitivity of the OClO ECD profiles to various spectral corrections: Rayleigh scattering, solar I_o effect, Ring effect, polarization, tilt effect, and wavelength shifts. Tables 3, 4, 5, and 6 display separately the positive and negative mean differences of the OClO ECD, relative ECD error, residual RMS and χ^2_{doas} respectively, together with the relative frequencies of these increments for each spectral correction. As an example, when the tilt correction is taken into account 71% of the OClO ECD increments are positive with a mean increase of 11% while 26% of the increments are negative with an mean difference value of −10% (see Table 3).

3.3.1. Rayleigh scattering

The spectral smoothing applied to obtain the differential quantities is performed by a second order closure polynomial in the 403–427 nm region. Rayleigh cross sections (from Bates, 1984) are included in the LSQ fit to complete the removal of this 4th order polynomial structure. This correction is especially important for the lower stratosphere where Rayleigh scattering is more efficient. The Rayleigh correction yields a mean increase of 27% in the OClO ECD for 50% of the cases, while it reduces the residual RMS by 1% for almost all the cases. In light of this, this correction is included in the retrieval process.

3.3.2. Solar I_o effect

The absorption cross sections of the trace gases used in the DOAS analysis are taken from the literature. OS spectra and laboratory absorption cross sections are measured at different spectral resolutions and using different light sources. In the case of limb-scattered sunlight measurements, the reference I_o spectrum is highly structured due to the presence of Fraunhofer lines whereas the I_o spectrum used to measure the

laboratory cross sections is nearly unstructured. Thus, the usually highly resolved laboratory cross sections σ_i^{hr} have to be convolved to the OS resolution including the so-called solar I_0 effect (Aliwell et al., 2002). For small optical depths, the solar I_0-corrected cross sections σ_i^* can be approximated as (Haley et al., 2004)

$$\sigma_i^*(\lambda) \approx \frac{\int_{-\infty}^{+\infty} g(\lambda', s_g) I_s^{hr}(\lambda - \lambda') \sigma_i^{hr}(\lambda - \lambda') d\lambda'}{\int_{-\infty}^{+\infty} g(\lambda', s_g) I_s^{hr}(\lambda - \lambda') d\lambda'}, \quad (10)$$

where I_s^{hr} is a solar exoatmospheric spectrum at a resolution identical to that of σ_i^{hr}, g is the instrumental filter function and s_g is the standard deviation of g. The following high-resolution and temperature-dependent cross sections are I_0 corrected and used in this study: a) O_3 from Bogumil et al. (2003) at temperatures 203 K, 223 K, 243 K, 273 K and 293 K with quadratic interpolation and resolution (FWHM) of 0.52 nm at 415 nm, b) NO_2 from Vandaele et al. (1998) at temperatures 200 K and 294 K with linear interpolation and resolution (FWHM) of 34 pm at 415 nm, c) OClO from Kromminga et al. (2003) at temperatures 213 K, 223 K, 253 K, 273 K and 293 K with quadratic interpolation and resolution (FWHM) of 17 pm at 415 nm, and d) O_4 from Greenblatt et al. (1990) at temperature 296 K and resolution (FWHM) of 0.56 nm. The difference between the uncorrected and I_0-corrected cross sections is larger for OClO (up to 4%) than for the interfering species in this fitting region. Accounting for the I_0 effect increases the OClO effective columns by an average of 8% in 64% of the cases while a reduction of 1% is observed in the residual RMS and χ^2_{doas} statistics. Moreover, the relative error decreases 8% in 69% of the cases. As a result, the I_0-corrected cross sections are used in this work.

ACPD
5, 2989–3046, 2005

3.3.3. Ring effect

The solar radiation in the Earth's atmosphere undergoes inelastic scattering by Rotational Raman Scattering (RRS). This scattering results from interactions between molecular rotation and electromagnetic waves and changes the frequency of the scattered light. RRS is proposed to be the most probable cause for the broadening and reduction of depth of the Fraunhofer lines, the so-called Ring effect. The magnitude of RRS is a function of pressure, temperature, aerosol, ground albedo and scattering angle. Thus, the RRS structure in the OS limb-scattered spectra varies with tangent height. As a consequence, the Fraunhofer lines of the measured spectra do not entirely cancel out when computing the DOD and could mask the weak absorption of some trace gases if the Ring effect is not properly accounted for. Before performing the DOAS LSQ fit, an iterative backward Ring model (Sioris et al., 2002) is used to remove the Ring effect from OS limb spectra. When the Ring effect is considered, the residual RMS are even larger and χ^2_{doas} values increase away from one for almost all the cases, indicating a poorer fit. This is consistent with the results found by Haley et al. (2004) and Sioris et al. (2003) when retrieving NO_2. An explanation for this could be that the 403–427 nm window does not contain strong Fraunhofer lines and the use of a high tangent height reference from within the scan leads to a large cancellation of the effect.

3.3.4. Polarization

Solar radiation becomes partially polarized when it is scattered by air molecules and aerosol particles in the Earth's atmosphere. Like most grating spectrometers, OS sensitivity is dependent on the polarization state of the light; this dependence is larger for incident light polarized perpendicular to the grooves of the grating. Since the scattering angle is often close to 90 degrees in the OSIRIS viewing geometry, the contribution of the perpendicular component is maximized. McLinden et al. (2002a) concluded that the linear polarization of OS limb radiances varies little for tangent heights larger than

30 km since the entire path is above both the ozone and aerosol layers. At lower tangent heights, multiple scattering and scattering by aerosols become more important and the variation of polarization is stronger. Figure 5 shows the OS polarization efficiency parameter in the 403–427 nm window computed as described by McLinden et al. (2002b). Because this parameter is not completely removed by a second order polynomial, it is included as a pseudo-absorber in the LSQ fit at all tangent heights in the sensitivity analysis. However, as the analysis shows, the polarization correction can be ignored since it has a negligible impact on the OClO columns and their relative errors as well as on the other statistics.

3.3.5. Tilt effect

The Fraunhofer lines observed in the reference tangent height spectrum and a lower tangent height spectrum can appear shifted and skewed to each other. This effect, denoted 'tilt effect', was discovered by Sioris et al. (2003) and is mainly explained by the undersampling of the OS spectra (~2 pixels/FWHM) in combination with Rayleigh and Mie trending (tilt) of the limb radiances. Because of the large efficiency of Rayleigh scattering in the short wave range, this effect is most pronounced in the UV and blue regions of the spectrum. This phenomenon can be roughly accounted for by introducing a pseudo-absorber in the DOAS LSQ fit (Sioris et al., 2003). If atmospheric absorption is ignored, the tilt pseudoabsorber $t(\lambda, h_t)$ is calculated as (Haley et al., 2004)

$$t(\lambda, h_t) = \frac{I^{os}(\lambda, h_t^{ref})/I^{os}(\lambda, h_t)}{I^{hr}(\lambda, h_t^{ref})/I^{hr}(\lambda, h_t)} - 1 \quad (11)$$

where the ratio of the spectra convolved to the OS resolution and sampling, I^{os}, is related to the ratio of highly resolved and sampled spectra, I^{hr}, and h_t^{ref} is the reference tangent height. In this study, the LIMBTRAN radiative transfer model (see Sect. 3.4.1) is used to simulate spectral limb radiances at different tangent heights under Antarctic spring conditions (large SZA and high ground albedo). A set of tilt pseudoabsorbers

ACPD
5, 2989–3046, 2005

is calculated at tangent heights between 10 and 40 km with a 2-km interval when the reference tangent height was set to 50 km. The pseudoabsorber at a specific tangent height h_t is linearly interpolated from this set of pre-calculated tilt pseudoabsorbers. Figure 6 displays the tilt pseudoabsorber at four tangent heights (i.e., 10, 20, 30 and 40 km) in the 403–427 nm window. The influence of this effect in the fit diminishes as h_t approaches h_t^{ref} since the slope difference of the spectra becomes smaller. A large improvement in the DOAS fit is observed for almost all the scans when the tilt effect is considered. The residual RMS decreases by as much as a factor of 1.5 whereas χ^2_{doas} diminishes 24% in average. The improvement of the fit also leads to larger OClO abundances in 71% of the cases with an average increase of 11%.

3.3.6. Wavelength shift

The wavelength calibration of OS has been determined by applying two methods. A Levenberg-Marquardt (L-M) (Levenberg, 1944; Marquardt, 1963) fit of a high resolution solar spectrum (Kurucz, http://kurucz.harvard.edu/sun/IRRADIANCE/irradiancebins.dat) to OS limb radiance spectra at mesospheric altitudes has been performed to the blue part of the spectrum. To the red end of the spectrum, the wavelength calibration was determined by using intense airglow features, Fraunhofer lines, and O_2 absorption features (Sioris and Haley, personal communication). However, this is only a nominal calibration and any wavelength misalignment between the measured limb-scattered radiance spectra and the absorption cross sections could affect the DOAS fit. An absolute shift in wavelength is determined through L-M non-linear iterations on the DOAS fit to the lowest tangent height measurement and then applied to all measurements in the scan. The fit minimizes the residuals with an emphasis on the dominant absorber (NO_2 in the 403–427 nm window). After processing the set of 122 scans, a 0.03 nm average shift was found, but with large standard deviations (i.e., 0.045 nm). As seen in Tables 3, 4, 5, and 6, the wavelength shift has no clear impact on the fit. It is likely that because of the low NO_2 concentration inside the polar vortex area, the derived shift is being dominated by the noise in the measurement. In light of this, the wavelength shift

ACPD
5, 2989–3046, 2005

is not applied when retrieving the OClO column densities.

3.3.7. Temperature dependence

The absorption cross sections of the trace gases are temperature dependent and the retrieved ECD could be influenced by the specific cross sections chosen for the fit. The Kromminga et al. (2003) OClO differential cross sections show a large temperature dependence varying by up to 40% between 213 and 233 K in the 403–427 wavelength interval. Since limb-scattered radiance spectra contain contributions from different tangent heights and the temperature varies with height, the effective temperature at which the absorption occurred for each spectrum is not obvious. If the temperature dependence is not properly taken into account (i.e., incorrect fixed temperature is assumed) and the use of the wrong cross sections in the DOAS fit will lead to the retrieval of the wrong ECD. However, as described in Sect. 3.4.1, a forward model is employed to invert the ECD to number density. Any systematic error in the ECD derived from the measurements will be compensated for when ECD are calculated from the model radiances, if the temperature profile and cross sections used in the radiative transfer model are correct and the same method for accounting for temperature dependence in the DOAS fit is applied in the forward model. As a consequence, the absorption cross sections were selected at fixed temperatures: 203 K for O_3 (Bogumil et al., 2003), NO_2 at 220 K (Vandaele et al., 1998), OClO at 213 K (Kromminga et al., 2003), and O_4 at 296 K (Greenblatt et al., 1990). Cross sections at the coldest temperatures available were chosen since the European Centre for Medium-range Weather Forecasts (ECMWF) analysis for 19–20 September 2002 suggests cold temperatures inside the polar vortex region (i.e., <200 K).

As a result of these sensitivity tests, Rayleigh scattering, I_o effect, tilt effect and fixed absorption cross sections are the spectral corrections applied when retrieving OClO in the 403–427 nm region. Figure 7 presents a typical OClO fit showing the fitted and observed OClO optical depths and the residual structures for scan 8565047 at 18.7 km

ACPD
5, 2989–3046, 2005

tangent height inside the polar vortex area.

3.4. Inversion

The objective of the inversion is to convert the OClO ECD as a function of tangent height, obtained from the DOAS analysis, to vertical number density profiles as a function of altitude. The problem is best approached with the use of a forward model $\boldsymbol{F}$ that relates the vector of OClO ECD for a set of tangent heights $\boldsymbol{c}$ to the number density vector $\boldsymbol{n}$ by

$$\boldsymbol{c}(h_t) = \boldsymbol{F}(\boldsymbol{n}, \boldsymbol{b}, h_t) + \varepsilon, \tag{12}$$

where $\boldsymbol{b}$ is the vector of model parameters that are not retrieved and ε is the measurement error.

The present inversion problem is ill-posed, under-constrained and non-linear. The problem is ill-posed because Eq. (12) does not have a unique solution. Hence, the inversion algorithm has to select a physically acceptable solution from a range of mathematically valid solutions (Jiménez et al., 2000). It is under-constrained because the number density profiles of OClO are continuous functions of altitude and the measurements were performed at discrete tangent heights. Additionally, since absorption is a linear process only for optically thin conditions, the problem becomes non-linear in the UV/blue region where the high Rayleigh scattering efficiency could lead to large optical depths at low tangent heights.

The inversion algorithm employed in this work is the maximum a posterior estimation method (Rodgers, 2000). MAP combines measurements with a priori information about the profile to find the best estimate of the true profile and its error covariance. This is done by maximizing the a posteriori probability density function of the state $\boldsymbol{n}$ given the measurement $\boldsymbol{c}$. If Gaussian statistics are assumed for variables and errors, the MAP estimator leads to the minimization of the following cost function J (Rodgers, 2000):

$$J(\boldsymbol{n}) = [\boldsymbol{c} - \boldsymbol{F}(\boldsymbol{n},\boldsymbol{b})]^T \mathbf{S}_\varepsilon^{-1} [\boldsymbol{c} - \boldsymbol{F}(\boldsymbol{n},\boldsymbol{b})] + [\boldsymbol{n} - \boldsymbol{n}_a]^T \mathbf{S}_a^{-1} [\boldsymbol{n} - \boldsymbol{n}_a], \tag{13}$$

where $\boldsymbol{n}_a$ is the a priori number density state vector, $\mathbf{S}_a$ is the a priori covariance matrix, and $\mathbf{S}_\varepsilon$ is the measurement error covariance matrix. $\mathbf{S}_\varepsilon$ is a diagonal matrix since ε is assumed to be uncorrelated in tangent height. In order to avoid negative values that could lead to unstable retrievals, the natural logarithm of the concentrations $\ln(\boldsymbol{n})$ is inverted instead of the concentrations $\boldsymbol{n}$. This positive constraint requires a non-linear retrieval.

If the inversion problem is linear the forward model can be expressed as $\boldsymbol{F}=\mathbf{K}\boldsymbol{n}$, where $\mathbf{K}$ is the weighting function matrix, and the minimization of J can be analytically solved. However, if the problem is not linear, it must be solved numerically and iteratively. To this end, a simplified Levenberg-Marquardt iterative scheme has been chosen to minimize J, yielding the following solution:

$$\boldsymbol{n}_{i+1} = \boldsymbol{n}_i + \left[(1+\gamma_i)\mathbf{S}_a^{-1} + \mathbf{K}_i^T\mathbf{S}_\varepsilon^{-1}\mathbf{K}_i\right]^{-1}\left[\mathbf{K}_i^T\mathbf{S}_\varepsilon^{-1}(\boldsymbol{c}-\boldsymbol{F}(\boldsymbol{n}_i,\boldsymbol{b})) - \mathbf{S}_a^{-1}(\boldsymbol{n}_i-\boldsymbol{n}_a)\right], \quad (14)$$

where the weighting function matrix $\mathbf{K}_i$ is calculated for each iteration step i (see Sect. 3.4.1) and γ_i determines the step size of the iteration. The simplified L-M method is a combination of the steepest descent and Gauss-Newton (G-N) methods where γ_i is the parameter controlling the balance between them (Rodgers, 2000).

Two different strategies were applied in this investigation. The first one is to find the solution within 10 iterations using the G-N method. When an occasional fail in convergence occurs, the L-M scheme is applied. Large γ_i values are set during the first iterations of L-M to descend with small steps. Once the solution is closer to the minimum, small γ_i values are chosen because the G-N iteration converges faster. The iteration is halted when the size of the step $(\boldsymbol{n}_{i+1}-\boldsymbol{n}_i)$ is smaller than the estimated error. Thus, the convergence criterion is expressed as

$$\frac{(\boldsymbol{n}_{i+1}-\boldsymbol{n}_i)^T\hat{\mathbf{S}}^{-1}(\boldsymbol{n}_{i+1}-\boldsymbol{n}_i)}{p} < \Delta n, \quad (15)$$

where p is the length of $\boldsymbol{n}$, Δn is the absolute convergence tolerance, and $\hat{\mathbf{S}}^{-1}$ can be approximated by

$$\hat{\mathbf{S}}^{-1}(\boldsymbol{n}_{i+1} - \boldsymbol{n}_i) \approx \mathbf{K}_i^T \mathbf{S}_\varepsilon^{-1} [\boldsymbol{c} - \boldsymbol{F}(\boldsymbol{n}_i, \boldsymbol{b})] - \mathbf{S}_a^{-1} [\boldsymbol{n}_i - \boldsymbol{n}_a] . \quad (16)$$

In this study, Δn is set to 0.001. Once Eq. (14) has converged to some value $\hat{\boldsymbol{n}}$ with corresponding $\hat{\mathbf{K}}$, a standard χ^2 test is carried out to determine whether the difference between the retrieved and measured quantities is statistically significant at some appropriate level. Following Rodgers (2000), the reduced chi-squared statistic for the inversion is defined by

$$\chi^2_{inv} = \frac{\left[\boldsymbol{c} - \boldsymbol{F}(\hat{\boldsymbol{n}}, \boldsymbol{b})\right]^T \mathbf{S}_{\delta\hat{c}}^{-1} \left[\boldsymbol{c} - \boldsymbol{F}(\hat{\boldsymbol{n}}, \boldsymbol{b})\right]}{q}, \quad (17)$$

where $\mathbf{S}_{\delta\hat{c}}=\mathbf{S}_\varepsilon \left[\hat{\mathbf{K}}\mathbf{S}_a\hat{\mathbf{K}}^T + \mathbf{S}_\varepsilon\right]^{-1} \mathbf{S}_\varepsilon$ is the covariance matrix of $\delta\hat{\boldsymbol{c}}=\boldsymbol{c} - \boldsymbol{F}(\hat{\boldsymbol{n}}, \boldsymbol{b})$ and q is the length of $\boldsymbol{c}$. The probability of obtaining a value of $\chi^2_{inv}>4$ is one in a million for a χ^2 distribution with 30 degrees of freedom. Hence, profiles following this condition are ruled out.

3.4.1. The forward model

A radiative transfer model (RTM) simulates the limb-scattered radiances to different tangent height for a specified wavelength range and a given vertical number density profile of the species of interest. The simulated optical depths are then calculated and subjected to a DOAS analysis. The resulting effective column densities constitute the forward model F. As described in Sect. 3.4, the forward model is used to invert ECD as a function of tangent height to number density as a function of altitude. Full spherical RTM models are not suitable for many repetitive calculations since they are slower than the simplified models. On the other hand, the error for models assuming a plane-parallel atmosphere is quite large in cases where SZA is larger than 75° (Herman et al.,

1994). Moreover, multiple scattering (MS) represents 10–50% of the total radiance at visible wavelengths in the limb viewing geometry, depending on SZA, SSA, albedo and tangent height (Oikarinen et al., 1999). The ratio MS/total radiance is even higher at SZA larger than 90°. In a trade-off between computational efficiency and accuracy, the pseudo-spherical multiple scattering radiative transfer model LIMBTRAN (Griffioen and Oikarinen, 2000) is applied in the inversion procedure. LIMBTRAN takes into account the variation of SZA and single scattering angle (SSA) along the LOS and assumes horizontal homogeneity within its vertical layers. Temperature and pressure data used in this RTM are from the ECMWF analysis fields. The O_3 mean state distribution is taken from the four-dimensional climatology of Li and Shine (1995) which is based on satellite and ozonesonde data sets. The NO_2 information is taken from a climatology constructed using the PRATMO photochemical box model (Prather and Jaffe, 1990; McLinden et al., 2000) that accounts for the diurnal variation of this species. The OClO a priori distribution is described in Sect. 3.4.2. The temperature-dependent cross sections employed in LIMBTRAN are the same as those used for the spectral fitting (see Sect. 3.3.2). A simple stratospheric aerosol model is included based on fitted parameters as a function of season and tropopause height (McCormick et al., 1996; McLinden et al., 2000). The ground albedo is derived from the climatology of GOME Lambertian-Equivalent Reflectivity of the Earth's surface (Koelemeijer et al., 2003). The reader is referred to Haley et al. (2004) for more details on the simulation of OS radiances with this model.

3.4.2. A priori information

The most satisfactory source of a priori information is from independent high spatial resolution measurements (Rodgers, 2000). However, a climatology of such measurements is not available for OClO. Thus, the a priori information is simulated with the REPROBUS chemical transport model (Lefèvre et al., 1994, 1998). This three-dimensional model takes into account the heterogeneous chemical reactions produced on the surface of the PSCs and extends from the ground up to 0.1 hPa on 42 levels.

In this work, the model was integrated from 1 July 2002 until 1 December 2002 in a 2° latitude by 2° longitude horizontal grid and 15-min time step. The kinetic and photochemical data are based on Sander et al. (2000) for this particular study. Temperatures, winds and ground pressure analyzed every 6 h by the ECMWF were employed in the simulations. The ozone field was initialized on 1 July 2002 from the three-dimensional ECMWF ozone analysis whereas other species were initialized from a June zonal mean computed from a REPROBUS long-term simulation. The generated vertical profiles are taken from the model grid points closest to the location and time of the selected OS measurements.

The OClO vertical distribution is assumed to be log-normal and the species variability is modelled by (Rodgers, 2000)

$$S_a(i,j) = \rho^2 \exp\left[\frac{-|z(i)-z(j)|}{l_c}\right], \tag{18}$$

where z is the altitude indexed by i and j, ρ is the standard deviation of the diagonal components, and l_c is the correlation length of the off-diagonal elements. A reliable climatology of the vertical OClO variability is essential to determine ρ and l_c. Since such a statistics do not exist, a sensitivity study was carried out by using different values of ρ (100%, 200%, 300%, and 400%) and l_c (3 km and 4 km). In a trade-off between vertical resolution and retrieval error, ρ was set to 300% and l_c to 4 km.

3.4.3. Weighting functions

K is the $q \times p$ weighting function matrix that represents the forward model response to changes in the atmospheric state. The rows of **K** are called weighting functions and the computation of the elements of **K** requires the derivation of the forward model:

$$K(i,j) = \frac{\partial F[\boldsymbol{n}, \boldsymbol{b}, h_t(i)]}{\partial n[z(j)]}, \tag{19}$$

where the forward model is evaluated at tangent height $h_t(i)$ and $n[z(j)]$ is the number density at altitude $z(j)$. The relationship between the derivatives of the RTM and the derivatives of $\boldsymbol{F}$ is not obvious because of the intermediate DOAS step. Hence, the weighting functions are determined numerically by using finite differences with sequential perturbation (5% in this case) of the elements of $\boldsymbol{n}$. An element of the **K** matrix is approximated as

$$K(i,j) \approx \frac{F\left[\tilde{\boldsymbol{n}}, \boldsymbol{b}, h_t(i)\right] - F\left[\boldsymbol{n}, \boldsymbol{b}, h_t(i)\right]}{\tilde{n}[z(j)] - n[z(j)]}, \tag{20}$$

where $\tilde{\boldsymbol{n}}$ is the perturbed number density vector.

This perturbation method is computationally expensive since the forward model has to be run p times to estimate **K** for every iteration. As a result, two simplifications have been implemented when calculating **K**. The first approximation is to reduce the number of spectral elements by using a two-wavelength DOAS approach as proposed by Haley et al. (2004). For the OClO retrieval in the 403–427 nm window, the wavelengths 412 and 409 nm were selected as the strong and weak OClO absorption wavelengths, respectively. This simplification does not lead to any significant differences when compared to a full DOAS analysis. The second simplification is to assume an aerosol-free atmosphere when simulating limb-scattered radiance spectra with the LIMBTRAN model. This approximation leads to negligible errors in the OClO retrievals. A selection of wavelengths is also applied to compute $\boldsymbol{F}$, and a 2 nm wavelength grid is found to be suitable in the 403–427 nm spectral range.

Figure 8 depicts the OClO weighting functions computed with these simplifications for spring Antarctic conditions. Each plotted profile exhibits how much the OClO ECD [molecule cm^{-2}] at a given tangent height would change if the number densities [molecule cm^{-3}] at the various profile levels were changed. For instance, if the OClO number density at 24 km were to increase by 1 molecule cm^{-3}, the OClO ECD at 24 km tangent height would increase by 6.7×10^{7} molecule cm^{-2}. The OClO ECD at tangent heights above 20 km are mostly influenced by OClO concentrations near

and slightly above the tangent point. The weighting functions show a pronounced step directly below the tangent height because the layers below have a small contribution in the limb viewing geometry. At lower tangent heights, the weighting functions become broader and peak around 22 km altitude, indicating contributions from higher altitudes than from the tangent point region. Due to the different shape of the weighting functions below 20 km, it is still possible to retrieve OClO down to 12 km of altitude. The rapid decrease observed in the weighting functions at low tangent heights is due to the increasing Rayleigh-scattering optical depths.

3.4.4. Error analysis

The total retrieval error is composed of the smoothing error, retrieval noise, forward model error, and forward model parameter error (Rodgers, 2000). The retrieval error can only be estimated on a statistical basis, using covariance matrices because the exact values of $\boldsymbol{n}$, $\boldsymbol{b}$, and ε are unknown (Jiménez et al., 2000). The limited vertical resolution of the observing system causes the smoothing error, whose covariance matrix $\mathbf{S}_s$ is calculated by

$$\mathbf{S}_s = (\mathbf{A} - \mathbf{1})\mathbf{S}_a(\mathbf{A} - \mathbf{1})^T, \tag{21}$$

where $\mathbf{A}$ is the averaging kernel matrix ($p \times p$) and $\mathbf{1}$ is the identity matrix. The $\mathbf{A}$ matrix is computed as $\mathbf{A}$=$\mathbf{GK}$ where $\mathbf{G}$ is the gain matrix defined as

$$\mathbf{G} = \mathbf{S}_a\mathbf{K}^T \left[\mathbf{K}\mathbf{S}_a\mathbf{K}^T + \mathbf{S}_\varepsilon\right]^{-1}. \tag{22}$$

The retrieval noise is usually the easiest component to estimate and its covariance is given by

$$\mathbf{S}_m = \mathbf{G}\mathbf{S}_\varepsilon\mathbf{G}^T. \tag{23}$$

The forward model error arises due to the imperfections and approximations of the forward model. The forward model parameter error is related to the parameters specified

ACPD
5, 2989–3046, 2005

in the RTM such as ground albedo, stratospheric aerosol loading, atmospheric pressure and temperature profiles, and absorption cross sections of the trace gases. The estimation of the forward model and forward model parameter errors is not carried out in this study. The total retrieved error covariance is obtained by adding the covariance matrices of the four error sources. Note that the covariance matrix of the solution, $\hat{\mathbf{S}}$, is the sum of $\mathbf{S}_s$ and $\mathbf{S}_m$.

3.4.5. Inversion characterization

The vertical resolution of the retrieval is characterized by the width of the averaging kernel functions, defined as the rows of the **A** matrix. In this work, the spread s (Backus and Gilbert, 1970) is used as a measure of this width

$$s(z) = 12\frac{\int (z-z')^2\mathbf{A}^2(z,z')dz'}{\left[\int |\mathbf{A}(z,z')|\,dz'\right]^2}, \quad (24)$$

where z is the altitude of the nominal peak of the averaging kernel function. The measurement response w is given by the area of the averaging kernel functions and evaluates the relative contribution of the measurements and a priori information to the retrieved profile. Values close to one indicate that most of the information comes from the measurement and thus the retrieval is considered to be efficient. In this study, an efficient retrieval is chosen to be characterized by w larger than 0.7.

Figure 9 illustrates the OClO averaging kernel functions, measurement response, spread, retrieval noise and smoothing error for limb spectra measured on 19 September 2002 over the Antarctic region. Between 14 and 18 km altitude, the averaging kernel functions peak at their corresponding altitude. This is consistent with the small smoothing error and low a priori contamination observed at the same altitudes. Hence, the vertical resolution approximates well the retrieval grid of 2 km for this altitude range. The averaging kernel for the 10 km level has a broad peak at the wrong altitude (i.e., 12 km). The measurements thus contain little useful information on this level as indicated by the low measurement response. The averaging kernel for the 12 km level

ACPD
5, 2989–3046, 2005

peaks at the correct altitude, but the contributions from the neighbouring levels cause larger smoothing errors and larger spread. The influence of the a priori information is however rather small since the measurement responses are larger than 0.8. All of the averaging kernels above 18 km have broad peaks at 18 km altitude yielding large values of spread and smoothing error and low measurement response. As a result, the error of the solution (denoted by S) increases quickly with altitude for these layers. Therefore, the altitude of good measurement sensitivity (i.e., $w>0.7$) lies between 12 and 20 km for the OClO retrievals. In this altitude range, the retrieval noise varies from 27 to 52% with a 2–5 km altitude resolution. This example is generally representative of the entire set of Antarctic OClO data measured on 19–20 September 2002.

Summarizing, Table 7 presents the specifications of the spectral window used to retrieve OClO in this study.

4. Comparison

Several difficulties arise when trying to validate the OClO vertical profiles. The high photolysis frequency prevents the build-up of appreciable concentrations of OClO during daylight. Therefore most measurements have been performed during twilight and at night. In OSIRIS' case, measurements are carried out only close to the terminator when the chlorine system is not in a steady state. As a consequence, the profiles are very sensitive to differences in time, location, viewing geometry and gradients along the LOS. Thus, a comparison with independent observations is difficult.

In order to assess whether the retrieval method is appropriate and produces reasonable results, the computed OClO vertical concentrations are tested in three ways: a) comparison to coincident OClO values simulated using the REPROBUS model initialized on 1 July 2002, b) comparison to OClO vertical profiles measured in Arctic balloon campaigns, and c) interpretation of the OS OClO abundances with respect to the atmospheric conditions in the lower stratosphere.

Figure 10 shows the a priori OClO profile, the observed OS OClO profile with its as-

ACPD
5, 2989–3046, 2005

sociated retrieval error and the coincident profile calculated by the REPROBUS model for scan 8565047 on 19 September 2002. Even though the profiles are displayed between 10 and 30 km altitude, the OClO measurement response is larger than 0.7 only between 12 and 20 km altitude. The REPROBUS profile peaks at 16 km of altitude while the OS maximum is observed at 18 km, with a difference between peak values of less than 3%. There is a good agreement between the modelled and observed OClO abundances within the retrieval error between 14 and 18 km. Similar agreements between measurements of OClO performed during the THESEO 2000 campaign and model calculations were found in the lower stratosphere (Rivière et al., 2003).

As already mentioned, a few OClO vertical profiles have been measured with other instruments inside the polar vortex area. Table 8 summarizes the peak value and corresponding altitude, location, date and time of the OClO measurements reported by Pommereau and Piquard (1994), Renard et al. (1997) and Rivière et al. (2003), and for OS scan 8565047. The altitude of the OClO peak value and the shape of the profiles (not shown) are similar while the concentration values differ depending on location and time. The maximum OClO number density from OS is larger than the peak value detected by Pommereau and Piquard (1994) inside the Arctic polar vortex. This is consistent with the larger OClO column found above Antarctica where the polar vortex is more persistent and colder, allowing the formation of PSCs over a longer period of time (e.g. Miller et al., 1999). On the other hand, nighttime OClO slant column abundances were found higher than diurnal measurements since photolysis is the main destruction mechanism for this species (e.g. Wahner et al., 1989). This is coherent with the lower OS OClO peak value compared to the maximum values retrieved by Renard et al. (1997) and Rivière et al. (2003).

Using the potential vorticity isoline of -48×10^{-6} K m^2 kg^{-1} s^{-1} at the 475 K isentropic level to define the edge of the polar vortex (e.g. Braathen et al., 1994), Fig. 11a shows the OS O_3 and NO_2 concentrations – retrieved following Haley et al. (2004) – inside (scan 8565047) and outside (scan 8565037) the polar vortex area. Figure 11b displays the OS OClO and ECMWF temperature profiles for scan 8565047. Due to their

low measurement response, OClO profiles outside the Antarctic vortex are not shown. Large OClO number densities are observed inside the polar vortex over areas where reduced O_3 and NO_2 number densities are also found. Low NO_2 concentrations in the ozone hole area are expected due to denitrification and denoxification processes that remove and sequester reactive nitrogen compounds. Temperatures below the threshold of the PSC formation (i.e., typically <196 K) are observed between 14 and 23 km of altitude where the largest OClO concentrations are detected. Thus, the OClO profile shows the expected relation to the atmospheric conditions in the lower stratosphere.

5. Results and conclusions

To illustrate the OS capabilities of OClO detection, two figures with OClO profiles as well as concentrations of other related species are presented. OClO ECD measurements along the Odin orbit 8565 on 19 September 2002 are shown in Fig. 12 (top panel) together with two number density profiles for two scans (middle panel) inside the ozone hole area. The bottom panel depicts the Southern Hemisphere total ozone content from EP/TOMS (http://jwocky.gsfc.nasa.gov/ozone/ozone_v8.html) for the same day. A clear core region of high OClO ECDs is observed in the region where the total ozone column is the lowest (i.e, <200 DU).

The mean OClO ECD for the orbit 8565 inside the polar vortex region is statistically significantly larger than the mean OClO ECD outside the vortex at 95% confidence level. The ECDs outside the vortex area are statistically significantly different from zero at 95% confidence level for the same orbit. However, these concentrations are very low and their location coincides with areas where very low abundances of OClO are expected. As a result, OClO number density retrievals are limited to chlorine activation regions. The morning OClO profile (scan A) peaks at 14 km with an estimated retrieval error of 52% while the evening profile (scan B) peaks at 16 km with an estimated retrieval error of 19%. The evening twilight concentrations are larger than the morning abundances, in accordance with the results found by several authors (e.g., Sanders et

al., 1989; Perner et al., 1991).

Figure 13 displays the number density profiles of O_3, NO_2, OClO, and ClO along the Odin orbit 8565 for latitudes south of 40° S. All of these measurements were performed at twilight conditions with SZA ranging from 91° to 92.1° when Odin was pointing off of the orbital plane into the sunlit region. O_3 and NO_2 profiles were derived from OS measurements according to Haley et al. (2004). The "SMR retrieval group" at "Chalmers University of Technology" retrieved the ClO profiles from Odin/SMR spectra (J. Urban, personal communication). The white lines in the plots indicate the lowermost and uppermost altitudes of significant measurements. A large ozone depletion is mainly detected between 16 and 30 km, associated with an important denitrification and denoxification of the lower stratosphere as shown by plots a) and b). This is consistent with an OClO enhancement observed in the 10–22 km altitude range where a cold temperature core is also found with temperatures lower than the PSC threshold formation (i.e, <196 K). An area with large ClO concentrations is observed at altitudes below 20 km (panel d), adhering well with the OClO abundances. The sunrise OClO concentrations are lower than the sunset abundances as depicted in panel c) since the diurnal variation is largely driven by the diurnal cycle of its photolysis rate (Solomon et al., 1990).

In summary, an algorithm for retrieving stratospheric OClO profiles from limb-scattered sunlight radiances has been described and applied to OS measurements. OClO profiles were retrieved inside the Antarctic polar vortex region with a measurement response above 0.7 and a vertical resolution of 2–5 km in the altitude range 12–20 km. The estimated retrieval error is better than 60% at the peak of these profiles. This unique data set of OClO profiles is very promising for the study of the seasonal and interannual variability of this species and for inter-hemispheric comparisons. Further characterization of the forward model and forward model parameter errors has to be carried out. Also, further comparisons with other OClO measurements are desirable for data validation.

ACPD
5, 2989–3046, 2005

Glossary of symbols

$*$	convolution.
$\sim$	perturbation.
$\hat{}$	MAP estimate.
χ^2_{doas}	DOAS reduced chi squared.
χ^2_{inv}	reduced chi squared of the inversion.
Δn	absolute convergence tolerance.
ε	measurement error of OS (STD) [photon cm^{-2} s^{-1} nm^{-1} ster^{-1}].
$\varepsilon_{\tau'_{obs}}$	error in τ'_{obs} (STD).
ε_I	measurement error of I (STD).
ε_{I_o}	measurement error of I_o (STD).
γ	step size of the iteration.
η	number of pixels in the spectral window.
λ	wavelength [nm].
ρ	STD of the a priori profile [molecule cm^{-3}].
σ	absorption cross section [cm^2 molecule^{-1}].
σ'	differential absorption cross sections [cm^2 molecule^{-1}].
τ	optical depth.
τ'	differential optical depth.
τ'_{obs}	observed differential optical depth.
τ_M	Mie optical depth.
τ_R	Rayleigh optical depth.
$\mathbf{A}$	averaging kernel matrix.
$\boldsymbol{b}$	forward model parameter.
c	effective column density [molecule cm^{-2}].
$\boldsymbol{c}$	effective column density profile.
d	degrees of freedom.
$\boldsymbol{F}$	forward model vector.

ACPD
5, 2989–3046, 2005

$\mathbf{G}$	gain matrix.
g	instrumental filter function.
h_r	highly resolved.
h_t	tangent height [km].
h_t^{ref}	tangent height of reference [km].
I	radiance [photon cm^{-2} s^{-1} nm^{-1} $ster^{-1}$].
I_o	radiance of unattenuated spectrum.
J	cost function.
$\mathbf{K}$	weighting function matrix.
l_c	correlation length [km].
m	number of species.
n	number density [molecule cm^{-3}].
$\boldsymbol{n}$	number density profile.
$\boldsymbol{n}_a$	a priori number density profile.
P	atmospheric pressure [hPa].
p	number of heights in $\boldsymbol{n}$.
p_{eff}	polarization effectivity pseudoabsorber.
q	number of tangent heights in $\boldsymbol{c}$.
$\boldsymbol{r}$	DOAS fitting residual.
r_{RMS}	residual RMS.
$\mathbf{S}$	covariance matrix of the solution.
$\mathbf{S}_a$	covariance matrix of the a priori.
$\mathbf{S}_\varepsilon$	covariance matrix of the measurement.
$\mathbf{S}_m$	covariance matrix of the retrieval noise.
$\mathbf{S}_s$	covariance matrix of the smoothing error.
s	spread.
T	temperature [K].
t	tilt pseudoabsorber.
w	measurement response.

ACPD

5, 2989–3046, 2005

z	altitude [km].
DN	data number.
DOAS	differential optical absorption spectroscopy.
DOD	differential optical depth.
ECD	effective column density.
FWHM	full width at half maximum.
G-N	Gauss-Newton.
IRI	infrared imager.
L-M	Levenberg-Marquardt.
LOS	line of sight.
LSQ	least squares.
LST	local solar time [hours].
MAP	maximum a posteriori.
MS	multiple scattering.
OE	optimal estimation.
OS	optical spectrograph.
OSIRIS	Optical Spectrograph and Infrared Imager System.
PSCs	polar stratospheric clouds.
RMS	root mean square.
RRS	rotational Raman scattering.
RTM	radiative transfer model.
SMR	Submillimetre and Millimetre Radiometer.
SSA	single scattering angle [°].
STD	standard deviation.
SZA	solar zenith angle [°].
UV	ultraviolet.

Acknowledgements. The first author thanks P. Eriksson for helpful comments to set up the a priori constraint in the OClO retrievals and J. Gumbel for valuable discussions on the manuscript. We also thank the SMR retrieval group at Chalmers University of Technology and

the Odin/OSIRIS team for making the ClO vertical profiles and OSIRIS level 1 data available, respectively. This work was supported by the Swedish National Space Board, Chalmers University of Technology, and the Canadian Space Agency. Odin is a Swedish-led satellite project funded jointly by Sweden (SNSB), Canada (CSA), Finland (Tekes) and France (CNES).

References

Aliwell, S. R., Van Roozendael, M., Johnston, P. V., et al.: Analysis of BrO in zenith-sky spectra: An intercomparison exercise for analysis improvement, J. Geophys. Res., 107(D14), 4199, doi:10.1029/2001JD000329, 2002.

Backus, G. E. and Gilbert, J. F.: Uniqueness in the inversion of inaccurate gross Earth data, Philos. Trans. R. Soc. London, Ser. A, 266, 123–192, 1970.

Bates, D. R.: Rayleigh scattering by air, Planet. Space Sci., 32(6), 785–790, 1984.

Bertaux, J., Mégie, G., Widemann, T., Chassefière, E., Pellinen, R., Kyrölä, E., Korpela, S., and Simon, P.: Monitoring of ozone trend by stellar occultations: The GOMOS instrument, Adv. Space Res., 11(3), 237–242, 1991.

Bogumil, K., Orphal, J., Homann, T., et al.: Measurements of molecular absorption spectra with the SCIAMACHY pre-flight model: Instrument characterization and reference data for atmospheric remote-sensing in the 230–2380 nm region, J. Photochem. Photobiol. A: Chem, 157, 167–184, doi:10.1016/S1010-6030(3)00062-5, 2003.

Bovensmann, H., Burrows, J. P., Buchwitz, M., Frerick, J., Noël, S., Rozanov, V. V., Chance, K. V., and Goede, A. P. H.: SCIAMACHY: Mission objectives and measurement modes, J. Atmos. Sci., 56(2), 127–150, 1999.

Braathen., G. O., Rummukainen, M., Kyrö, E., Schmidt, U., Dahlback, A., Jørgersen, T. S., Fabian, R., Rudakov, V. V., Gil, M., and Borchers, R.: Temporal development of ozone within the Arctic vortex during the winter of 1991/92, Geophys. Res. Lett., 21(13), 1407–1410, 1994.

Brandtjen, R., Klüpfel, T., and Perner, D.: Airborne measurements during the European Arctic Stratospheric Ozone Experiment: Observation of OClO, Geophys. Res. Lett., 21(13), 1363–1366, 1994.

Farman, J. C., Gardiner, G., and Shanklin, J. D.: Large ozone losses of total ozone in Antarctica reveal seasonal ClO_x/NO_x interaction, Nature, 315, 207–210, 1985.

Frisk, U., Hagström, M., Ala-Laurinaho, S., et al.: The Odin satellite I: Radiometer design and test, Astron. Astrophys., 402(3), L27-L34, doi:10.1051/0004-6361:20030335, 2003.

Greenblatt, G. D., Orlando, J. J., Burkholder, J. B., and Ravinshankara, A. R.: Absorption measurements of oxygen between 300 and 1140 nm, J. Geophys. Res., 95(D11), 18 577–18 583, 1990.

Griffioen, E. and Oikarinen, L.: LIMBTRAN: A pseudo three-dimensional radiative transfer model for the limb-viewing imager OSIRIS on the Odin satellite, J. Geophys. Res., 105(D24), 29 717–29 730, 2000.

Haley, C. S., Brohede, S. M., Sioris, C. E., Griffioen, E., Murtagh, D. P., McDade, I. C., Eriksson, P., Llewellyn, E. J., Bazureau, A., and Goutail, F.: Retrieval of stratospheric O_3 and NO_2 profiles from Odin Optical Spectrograph and Infrared Imager System (OSIRIS) limb-scattered sunlight measurements, J. Geophys. Res., 109(D16303), doi:10.1029/2004JD004588, 2004.

Herman, B. M., Ben-David, A., and Thome, K. J.: Numerical technique for solving the radiative transfer equation for a spherical shell atmosphere, Appl. Opt., 33, 1760–1770, 1994.

Jiménez, C., Eriksson, P., and Askne, J.: Non-linear inversions of Odin sub-mm observations in the lower stratosphere by neural networks, in: Microwave Radiometry and Remote Sensing of the Earth's Surface and Atmosphere, VSP, Zeist, Netherlands, 503–511, 2000.

Koelemeijer, R. B. A., de Haan, J. F., and Stammes, P.: A database of spectral surface reflectivity in the range 335–772 nm derived from 5.5 years of GOME observations, J. Geophys. Res., 108(D2), 4070, doi:10.1029/2002JD002429, 2003.

Kromminga, H., Orphal, J., Spietz, P., Voigt, S., and Burrows, J. P.: New measurements of OClO absorption cross sections in the 325–435 nm and their temperature dependence between 213–293 K, J. Photochem. Photobiol. A.: Chem, 157, 149–160, 2003.

Lefèvre, F., Brasseur, G. P., Folkins, I., Smith, A. K., and Simon, P.: Chemistry of the 1991-1992 stratospheric winter: Three-dimensional model simulations, J. Geophys. Res., 99(D4), 8183–8195, 1994.

Lefèvre, F., Figarol, K., Carslaw, S., and Peter, T.: The 1997 Arctic ozone depletion quantified from three-dimensional model simulations, Geophys. Res. Lett., 25, 2425–2428, 1998.

Levenberg, K.: A method for the solution of certain problems in least-squares, Q. Appl. Math., 2, 164–168, 1944.

Li, D. and Shine, K. P.: A 4-dimensional ozone climatology for UGAMP models, UGAMP internal report 35, UK Univ. Global Atmos. Modell. Programme, Reading, 1995.

Llewellyn, E. J., Lloyd, N. D., Degenstein, D. A., et al.: The OSIRIS instrument on the Odin spacecraft, Can. J. Phys., 82(6), 411–422, doi:10.1139/P04-005, 2004.

Marquardt, D.: An algorithm for least-squares estimation on non-linear parameters, SIAM J. Appl. Math., 11, 431–441, 1963.
McCormick, M. P., Chu, W. P., Zawodny, J. M., Mauldin III, L. E., and McMaster, L. R.: Stratospheric Aerosol and Gas Experiment III (SAGE III) aerosol and trace gas measurements for Earth Observing System (EOS), Proc. SPIE Int. Soc. Opt. Eng., 1491, 125–141, 1991.
McCormick, M. P., Wang, P. H., and Pitts, M. C.: Background stratospheric aerosol and polar stratospheric cloud reference models, Adv. Space Res., 18(9-10), 155–177, 1996.
McLinden, C. A., Olsen, S., Hannegan, B., Wild, O., Prather, M. J., and Sundet, J.: Stratospheric ozone in 3-D models: A simple chemistry and the cross-tropopause flux, J. Geophys. Res., 105(D11), 14 653–14 665, 2000.
McLinden, C. A., McConnell, J. C., Griffioen, E., and McElroy, C. T.: A vector radiative-transfer model for the Odin/OSIRIS project, Can. J. Phys., 80(4), 375–393, 2002a.
McLinden, C. A., McConnell, J. C., Strong, K., McDade, I. C., Gattinger, R. L., King, R. Solheim, B., Llewellyn, E. J., and Evans, W. F. J.: The impact of the OSIRIS grating efficiency on radiance and trace-gas retrievals, Can. J. Phys., 80(4), 469–481, 2002b.
Miller, H. L., Saunders, R. W., and Solomon, S.: Observations and interpretation of column OClO seasonal cycles at two polar sites, J. Geophys. Res., 104(D15), 18 769–18 783, 1999.
Murtagh, D., Frisk, U., Merino, F., et al.: An overview of the Odin atmospheric mission, Can. J. Phys., 80(4), 309–319, 2002.
Noxon, J. F.: Nitrogen dioxide in the stratosphere and troposphere measured by ground-based absorption spectroscopy, Science, 189, 547–549, 1975.
Noxon, J. F., Whipple, E. C., and Hyde, R. S.: Stratospheric NO_2 I. Observational method and behavior at mid-latitude, J. Geophys. Res., 28(8), 5047–5065, 1979.
Oikarinen, L., Sihvola, E., and Kyrölä, E.: Multiple scattering radiance in limb-viewing geometry, J. Geophys. Res., 104(D24), 31 261–31 274, 1999.
Payan, S., Camy-Peyret, C., Jeseck, P., et al.: HALOMAX results on reservoir and active chlorine species: Ballon measurements and comparison with 3-D chemical transport model, stratospheric ozone 1999, in: Proceedings of the fifth European symposium, 27 September to 1 October 1999, Saint Jean de Luz, France, 1999.
Perner, D., Klüpfel, T., Parchatka, U., Roth, A., and Jørgensen, T.: Ground-based UV-VIS spectroscopy: Diurnal OClO profiles during January 1990 above Søndre Strømfjord, Greenland, Geophys. Res. Lett., 18(4), 787–790, 1991.
Perner, D., Roth, A., and Klüpfel, T.: Groundbased measurements of stratospheric OClO, NO_2,

and O_3 at Søndre Strømfjord in winter 1991/92, Geophys. Res. Lett., 21(13), 1367–1370, 1994.
Platt, U., Perner, D., and Pätz, H. W.: Simultaneous measurement of atmospheric CH_2O, O_3 and NO_2 by differential optical absorption, J. Geophys. Res., 84(10), 6329–6335, 1979.
Platt, U.: Differential optical absorption spectroscopy (DOAS), in: Air Monitoring by Spectroscopic Techniques, edited by: Sigrist, M., 27–84 pp., John Wiley, Hoboken, N.J., 1994.
Pommereau, J. P. and Piquard, J.: Observations of the vertical distribution of stratospheric OClO, Geophys. Res. Lett., 21(13), 1231–1234, 1994.
Prather, M. and Jaffe, A. H.: Global impact of the Antarctic ozone hole: Chemical propagation, J. Geophys. Res., 95(D4), 3473–3492, 1990.
Renard, J. B., Lefèvre, F., Pirre, M., Robert, C., and Huguenin, D.: Vertical profile of night-time stratospheric OClO, J. Atmos. Chem., 26, 65–76, 1997.
Rivière, E. D., Pirre, M., Berthet, G., Renard, J.-B., Taupin, F. G., Huret, N., and Chartier, M.: On the interaction between nitrogen and halogen species in the Arctic polar vortex during THESEO and THESEO 2000, J. Geophys. Res., 108(D5), 8311, doi:10.1029/2002JD002087, 2003.
Rodgers, C. D.: Inverse Methods for Atmospheric Sounding: Theory and Practice, 1st ed., World Sci., River Edge, N. J., 2000.
Sander, S. P., Friedl, R. R., DeMore, W. B., et al.: Chemical kinetics and photochemical data for use in stratospheric modeling, Evaluation number 13, JPL Publication 00-03, 2000.
Sanders, R. W., Solomon, S., Carroll, M. A., and Schmeltekopf, A. L.: Visible and near-ultraviolet spectroscopy at McMurdo station, Antarctica, 4. Overview and daily measurements of NO_2, O_3, and OClO during 1987, J. Geophys. Res., 94(D9), 11 381–11 391, 1989.
Schiller, C., Wahner, A., Platt, U., Dorn, H., Callies, J., and Ehhalt, D. H.: Near UV atmospheric absorption measurements of column abundances during airborne Arctic Stratospheric Expedition, January–February 1989: 2. OClO observations, Geophys. Res. Lett., 17(4), 501–504, 1990.
Sessler, J., Chipperfield, M. P., Pyle, J. A., and Tuomi, R.: Stratospheric OClO measurements as a poor quantitative indicator of chlorine activation, Geophys. Res. Lett., 22(6), 687–690, 1995.
Sioris, C. E., Evans, W. F. J., Gattinger, R. L., McDade, I. C., Degenstein, D. A., and Llewellyn, E. J.: Ground-based Ring-effect measurements with the OSIRIS development model, Can. J. Phys., 80 (4), 483–491, 2002.

Sioris, C. E., Haley, C. S., McLinden, C. A., et al.: Stratospheric profiles of nitrogen dioxide observed by Optical Spectrograph and Infrared Imager System on the Odin satellite, J. Geophys. Res., 108(D7), 4215, doi:10.1029/2002JD002672, 2003.

Solomon, S., Mount, G. H., Sanders, R. W., and Schmeltekopf, A. L.: Visible spectroscopy at McMurdo Station, Antarctica, 2. Observations of OClO, J. Geophys. Res., 92(D7), 8329–8338, 1987.

Solomon, S., Sanders, R. W., and Miller, H. L.: Visible and near-ultraviolet spectroscopy at McMurdo Station, Antarctica 7. OClO diurnal photochemistry and implications for ozone destruction, J. Geophys. Res., 95(D9), 13 807–13 817, 1990.

Solomon, S.: Stratospheric ozone depletion: A review of concepts and history, Rev. Geophys., 37(3), 275–316, 1999.

Van Roozendael, M., Hermans, C., Kabbadj, Y., Lambert, J.-C., Vandaele, A.-C., Simon, P. C., Carleer, M., Guilmot, J.-M., and Colin, R.: Ground-based measurements of stratospheric OClO, NO_2, and O_3 at Harestua, Norway (60° N, 10° E) during SESAME, in: Proceedings of 12th ESA Symposium on Rocket and Balloon Programmes & Related Research, Lillehammer, Norway, 29 May–1 June 1995, Eur. Space Agency Spec. Publ., ESA, SP-370, 305–310, 1995.

Vandaele, A., Hermans, C., Simon, P., Carleer, M., Colin, R., Fally, S., Mérienne, M. F., Jenouvrier, A., and Coquart, B.: Measurements of the NO_2 absorption cross section from 42 000 cm^{-1} to 10 000 cm^{-1} (283–1000 nm) at 220 K and 294 K, J. Quant. Spectrosc. Radiat. Transfer, 59(3-5), 171–184, 1998.

Wagner, T., Leue, C., Pfeilsticker, K., and Platt, U.: Monitoring of the stratospheric chlorine activation by Global Ozone Monitoring Experiment (GOME) OClO measurements in the austral and boreal winters 1995 through 1999, J. Geophys. Res., 106(D5), 4971–4986, 2001.

Wahner, A., Jakoubek, R. O., Mount, G. H., Ravishankara, A. R., and Schmeltekopf, A. L.: Remote sensing observations of nighttime OClO column during the Airborne Antarctic Ozone Experiment, September 8, 1987, J. Geophys. Res., 94(D9), 11 405–11 411, 1989.

Wilmouth, D. M., Hanisco, T. F., Donahue, N. M., and Anderson, J. G.: Fourier transform ultraviolet spectroscopy of the A2PI3/2–X2PI3/2 transition of BrO, J. Phys. Chem. A, 103, 8935–8945, 1999.

WMO (World Meteorological Organization): Scientific Assessment of Ozone Depletion: 2002, Global Ozone Research and Monitoring Project, Report No. 47, 498 pp., Geneva, 2003.

Table 1. Summary of the mission, spectral intervals and target species of the instruments onboard the Odin satellite.

Instrument	Mission	Interval	Target species (aeronomy)
SMR	astronomy/ aeronomy	486.1–503.9 GHz 541.0–580.4 GHz	O_3, N_2O, ClO, HNO_3, H_2O, CO, temperature.
OS	aeronomy	280–800 nm	O_3, NO_2, OClO, BrO, aerosols, noctilucent cloud properties, temperature.
IRI	aeronomy	1.27 and 1.53 μm	O_2 and OH airglows, mesospheric O_3, subvisible cirrus properties.

Table 2. Investigated spectral fitting windows for the OClO retrievals.

Window [nm]	η	Excluded λ [nm]	Interfering species
363–391	71	–	O_3, NO_2, O_4, BrO
403–427	61	–	O_3, NO_2, O_4
363–427	142	390.9–398.4	O_3, NO_2, O_4, BrO

ACPD
5, 2989–3046, 2005

Table 3. Positive and negative mean differences of OClO ECD and their relative frequencies when including each of these spectral corrections: Rayleigh, I_o, Ring, tilt, polarization and wavelength shift.

	Positive differences		Negative differences	
Correction	Mean [%]	Frequency [%]	Mean [%]	Frequency [%]
Rayleigh	27	50	−31	31
I_o	8	64	−13	32
Ring	32	59	−45	18
Tilt	11	71	−10	26
Polarization	3	61	−4	38
λ−shift	11	43	−11	45

Table 4. Positive and negative mean differences of OClO ECD relative error and their relative frequencies when including each of these spectral corrections: Rayleigh, I_o, Ring, tilt, polarization and wavelength shift.

	Positive differences		Negative differences	
Correction	Mean [%]	Frequency [%]	Mean [%]	Frequency [%]
Rayleigh	25	35	−26	47
I_o	14	28	−8	69
Ring	47	10	−29	73
Tilt	8	25	−10	73
Polarization	4	39	−3	60
λ−shift	10	48	−11	45

ACPD
5, 2989–3046, 2005

Table 5. Positive and negative mean differences of residual RMS and their relative frequencies when including each of these spectral corrections: Rayleigh, I_o, Ring, tilt, polarization and wavelength shift.

	Positive differences		Negative differences	
Correction	Mean [%]	Frequency [%]	Mean [%]	Frequency [%]
Rayleigh	0.1	3	−1	97
I_o	1	43	−1	57
Ring	4	97	−1	1
Tilt	0	0	−12	100
Polarization	0.1	3	−1	97
λ−shift	4	51	−2	47

ACPD
5, 2989–3046, 2005

Table 6. Positive and negative mean differences of reduced chi squared and their relative frequencies when including each of these spectral corrections: Rayleigh, I_o, Ring, tilt, polarization and wavelength shift.

	Positive differences		Negative differences	
Correction	Mean [%]	Frequency [%]	Mean [%]	Frequency [%]
Rayleigh	1	66	−3	34
I_o	2	44	−1	56
Ring	9	97	−2	1
Tilt	1	13	−24	87
Polarization	1	70	−3	30
λ−shift	8	51	−4	47

ACPD
5, 2989–3046, 2005

Table 7. Summary of the specifications of the spectral window used to retrieve OClO.

Retrievals	OClO window
Wavelengths	403–427 nm
Fitted species	O_3, NO_2, OClO, O_4
Closure polynomial	2nd order
Spectral corrections	Rayleigh, I_o, tilt, fixed cross sections
Retrieval range	10–40 km
Reference spectrum height	40–70 km average
Estimating **K**	2λ, MS, no aerosol
Estimating ***F***	2-nm grid
A priori STD	300%
Correlation length	4 km

ACPD
5, 2989–3046, 2005

Table 8. Observations of maximum OClO vertical concentrations.

Reference	Altitude [km]	n [cm^{-3}]	Location	Date	Time
Pommereau and Piquard (1994)	21	1.4×10^{7}	68° N, 20° E	Jan. 92	twilight, SZA 93°
Renard et al. (1997)	19	8.7×10^{7}	68° N, 20° E	Feb. 95	night
Rivière et al. (2003)	18	8.7×10^{7}	68° N, 22° E	Jan. 00	night
OSIRIS (scan 8565047)	18	7.3×10^{7}	82° S, 36° E	Sep. 02	twilight, SZA 92°

ACPD
5, 2989–3046, 2005

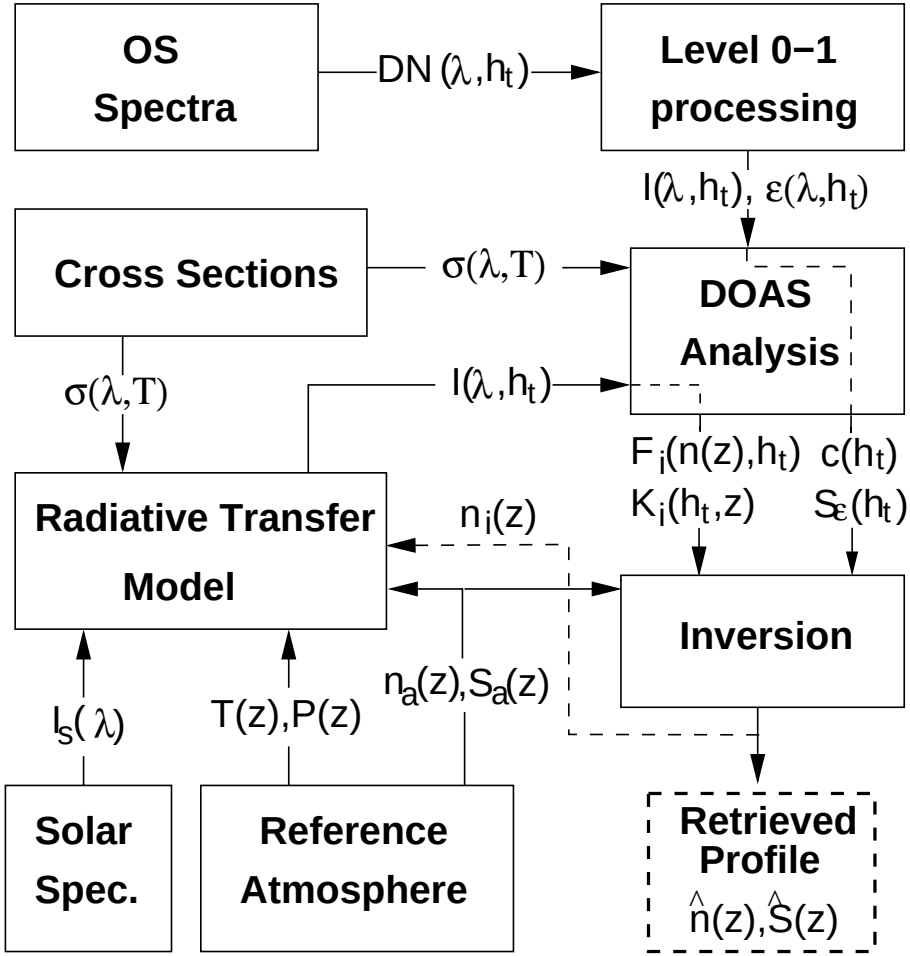

Fig. 1. Schematic description of the retrieval process.

ACPD
5, 2989–3046, 2005

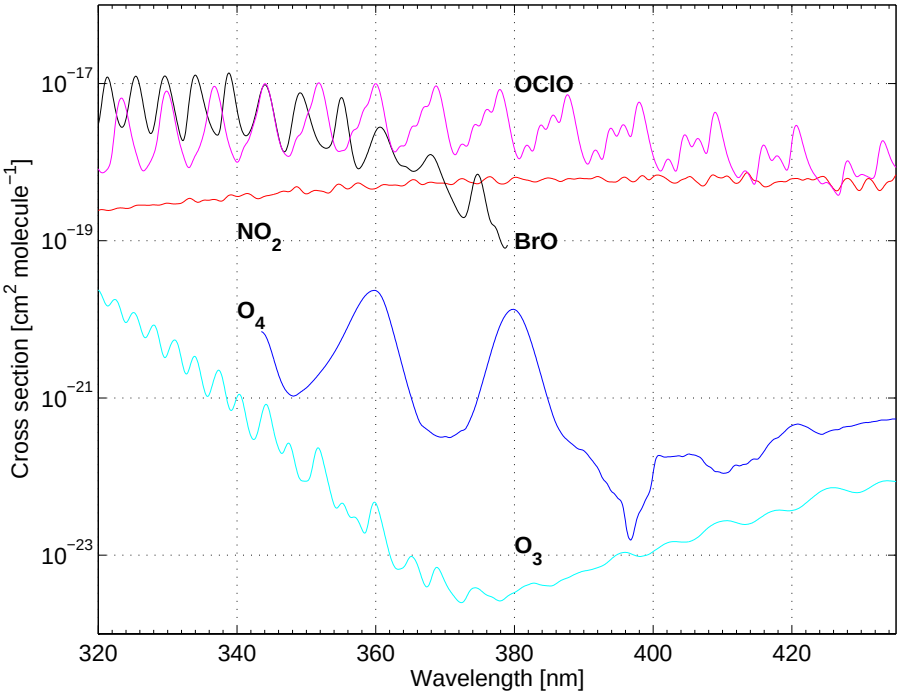

Fig. 2. Absorption cross sections of O_3 (Bogumil et al., 2003), NO_2 (Vandaele et al., 1998), OClO (Kromminga et al., 2003), BrO (Wilmouth et al., 1999), and O_4 (Greenblatt et al., 1990) convolved to the OS spectral resolution in the 320–435 nm region. O_4 cross sections have been multiplied by 10^7 to fit on the same scale.

ACPD
5, 2989–3046, 2005

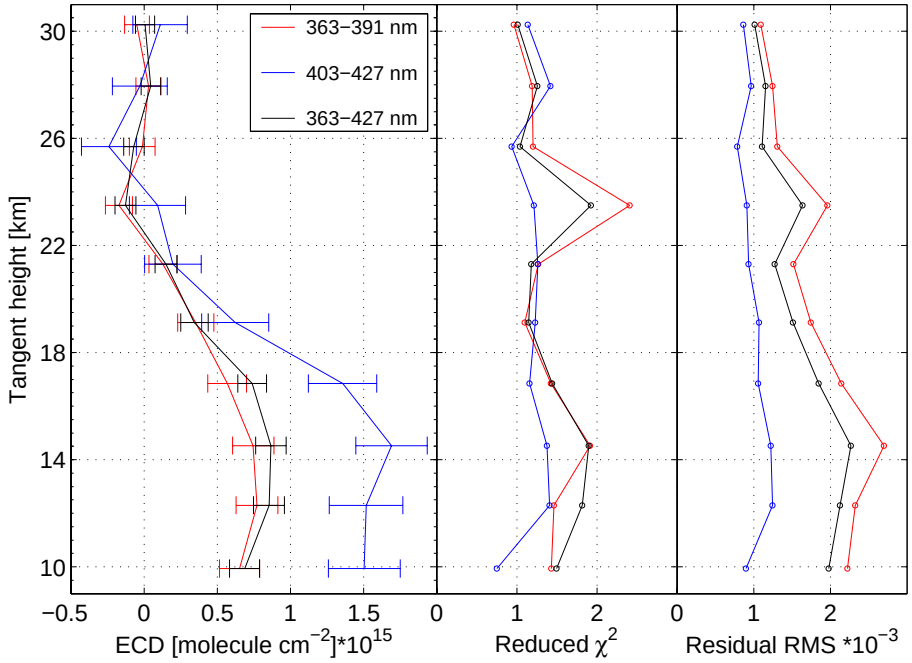

Fig. 3. Left panel: OClO ECD profiles retrieved from OSIRIS spectra measured on 19 September 2002 (scan 8567046, latitude 79.2° S, longitude 18.2° W, SZA 91.0°, 17:47 LST) in the 363–391 nm, 403–427 nm, and 363–427 nm fitting windows. The error bars represent the uncertainties of the LSQ fit. Middle panel: reduced chi squared. Right panel: residual RMS.

ACPD
5, 2989–3046, 2005

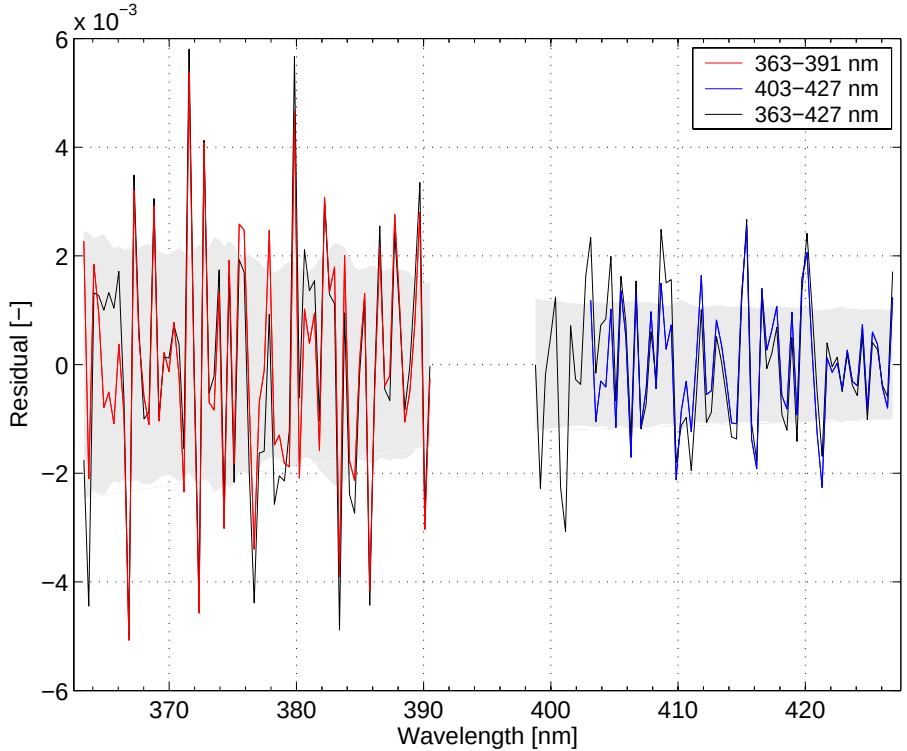

Fig. 4. Residual absorption spectra of scan 8567046 at the tangent height of 16.8 km in the wavelength regions: 363–391, 403–427, and 363–427 nm. The shaded region represents the estimated 1-STD error in the observed differential optical depth.

ACPD
5, 2989–3046, 2005

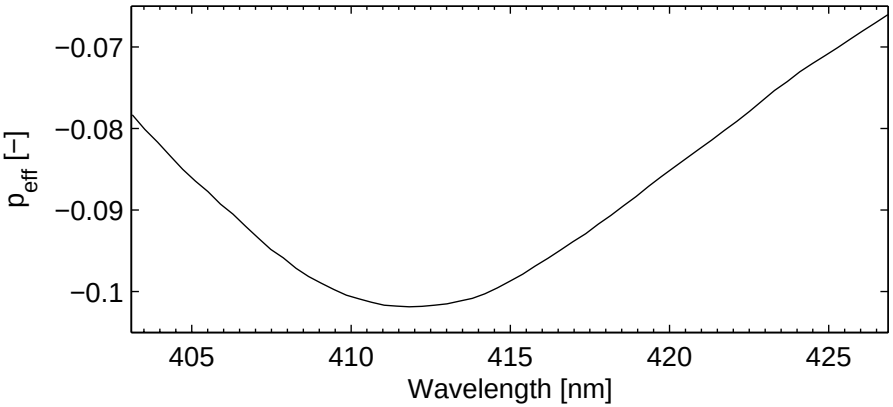

Fig. 5. OS polarization efficiency parameter p_{eff} in the 403–427 nm window.

ACPD
5, 2989–3046, 2005

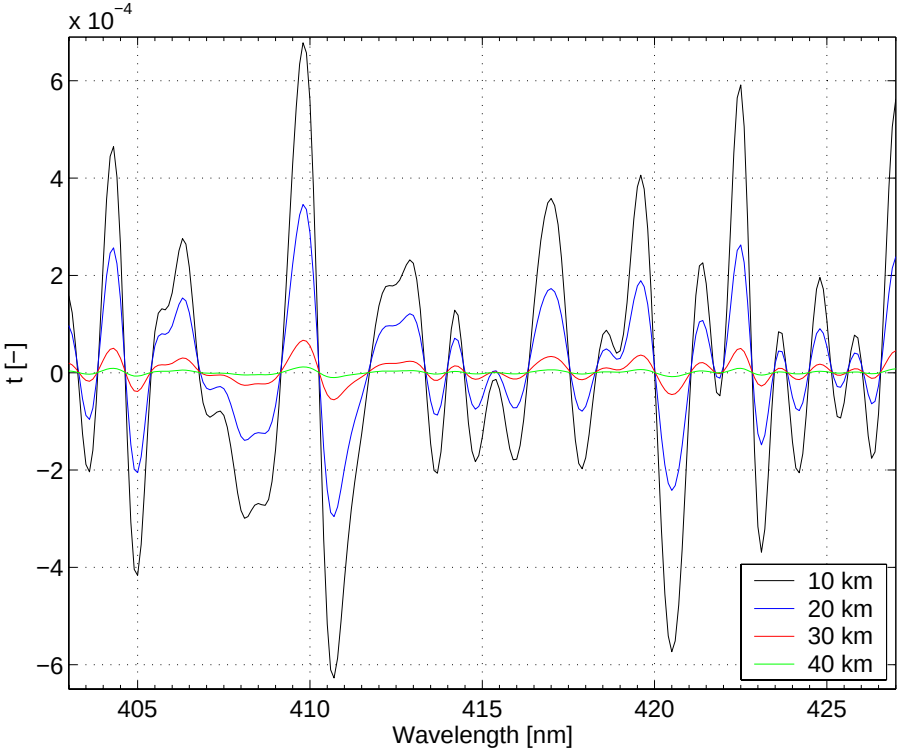

Fig. 6. Simulated tilt pseudoabsorber at 10, 20, 30, and 40 km tangent height in the spectral interval 403–427 nm.

ACPD
5, 2989–3046, 2005

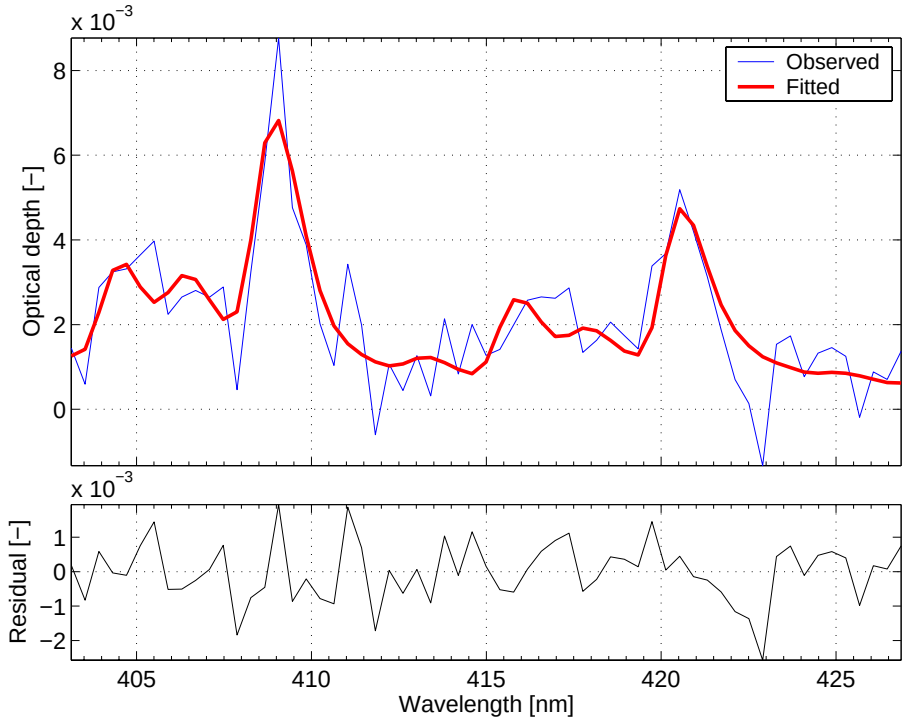

Fig. 7. Typical example of the fitted and observed optical depths of OClO and residual structures in the 403–427 nm region. The corresponding OS measurement was performed at 18.7 km tangent height on 19 September 2002 (scan 8565047, latitude 81.7° S, longitude 36.4° E, SZA 92.0°, 18:10 LST).

ACPD
5, 2989–3046, 2005

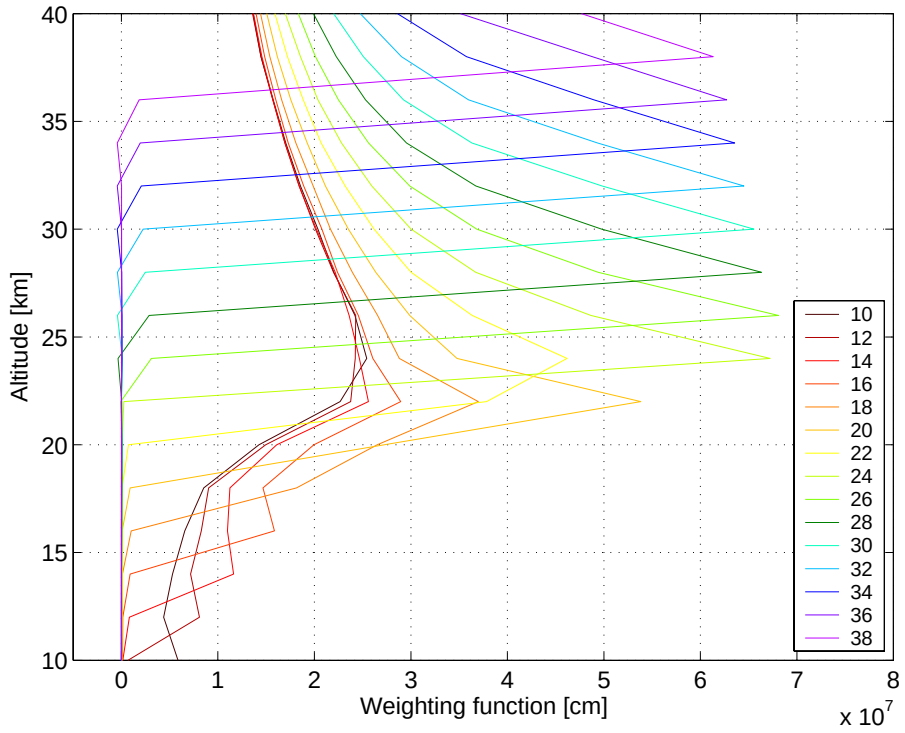

Fig. 8. OClO weighting functions for DOAS effective column densities calculated by using radiances at 409 and 412 nm, 5% perturbation, SZA 91°, SSA 72°, ground albedo 0.8, multiple scattering and no aerosols. Tangent heights are expressed in km.

ACPD
5, 2989–3046, 2005

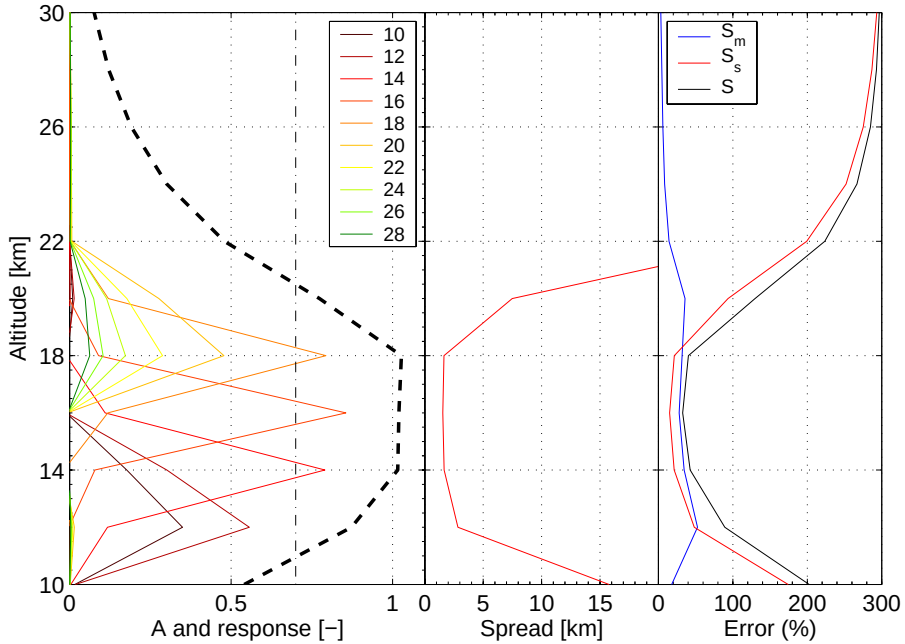

Fig. 9. Left panel: OClO averaging kernel functions with corresponding tangent heights given in km, measurement response w (dashed line), and w=0.7 (dashed-dotted line) for limb spectra measured on 19 September 2002 (scan 8567045, latitude 83.9° S, longitude 18.5° W, SZA 91°, SSA 72°, 17:44 LST). l_c was set to 4 km and ρ to 300%. Middle panel: spread s. Right panel: OClO number density errors: retrieval noise S_m, smoothing error S_s, and retrieval error S=S_m+S_s.

ACPD
5, 2989–3046, 2005

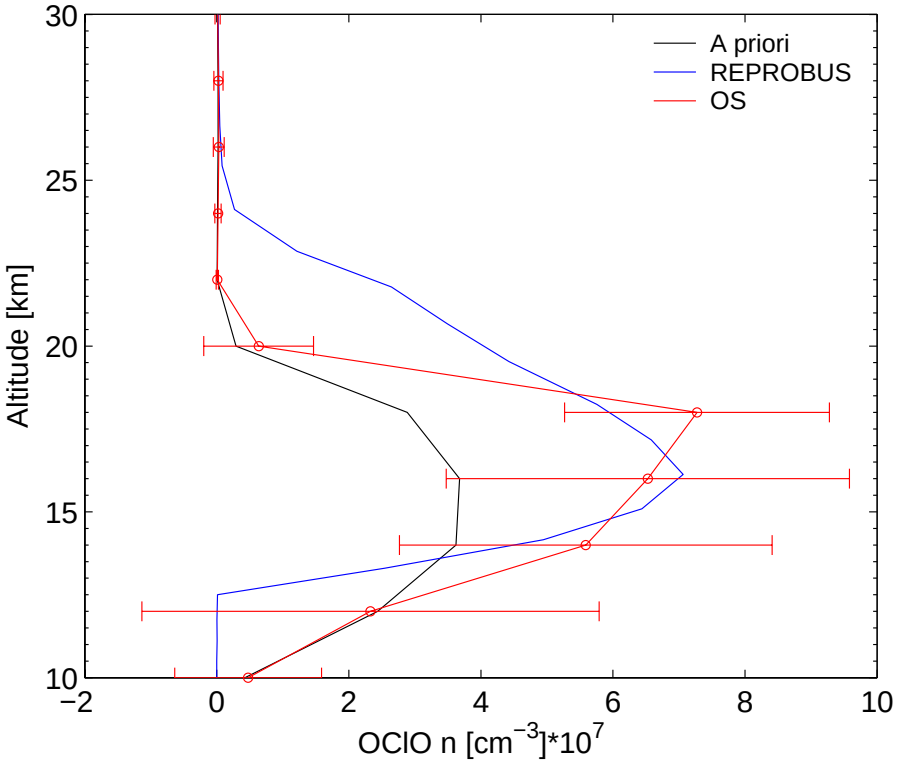

Fig. 10. OS OClO profile (scan 8565047, latitude 81.7° S, longitude 36.4° E, SZA 92.0°, 18:10 LST), and the coincident profile calculated by REPROBUS model (SZA 92.2°). The a priori profile and the error bars of the estimated OS retrieval error are also shown.

ACPD
5, 2989–3046, 2005

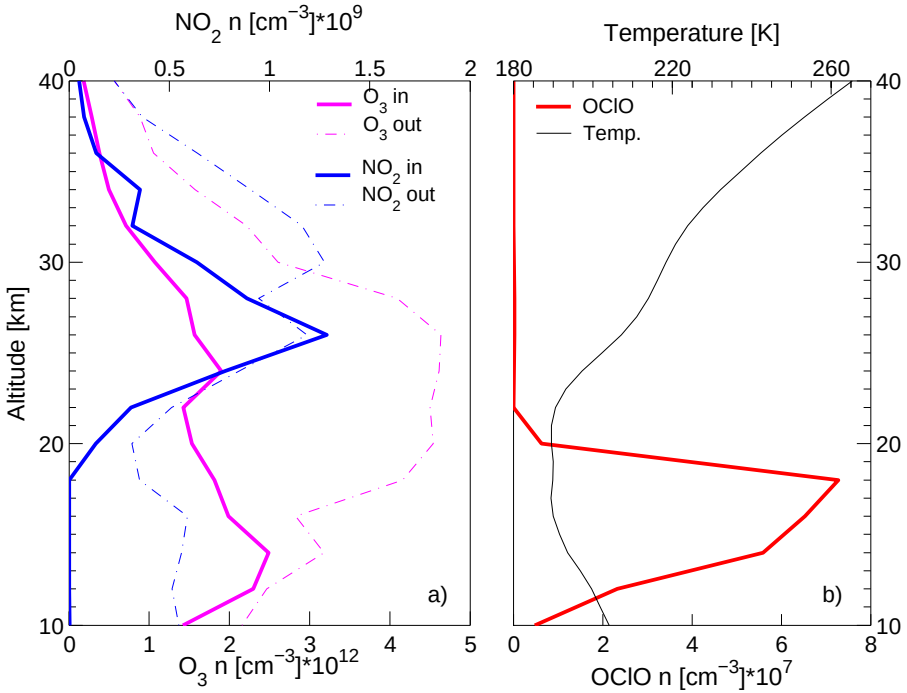

Fig. 11. (a) OS O_3 and NO_2 number density profiles inside (scan 8565047) and outside (scan 8565037, latitude 45.1° S, longitude 145.7° W, SZA 91.9°, 5:48 LST) the polar vortex region. **(b)** OS OClO number density and ECMWF temperature profiles for scan 8565047.

ACPD
5, 2989–3046, 2005

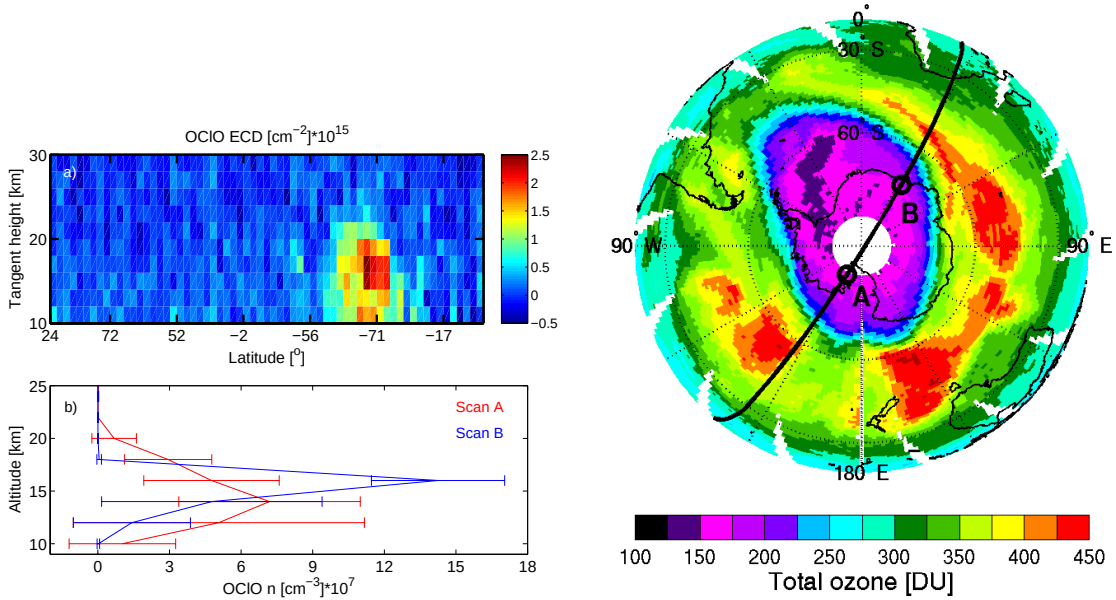

Fig. 12. Left panel: **(a)** Latitude vs. tangent height representation of OClO ECD along the orbit 8565 on 19 September 2002 and **(b)** OClO number density profiles for scans A (number 8565044, latitude 81.9° S, longitude 152.4° W, SZA 92.1°, 5:31 LST) and B (number 8565049, latitude 71.1° S, longitude 32.8° W, SZA 91.8°, 18:00 LST) with their corresponding retrieval error. Right panel: Austral total O_3 from EP/TOMS for the same day. The thick black line represents the OS tangent point path for orbit 8565, A and B indicate the average location of scans A and B, and the arrow shows the direction of Odin's movement. Sectors without measurements are not coloured. Note that Odin was pointing off of the orbit plane to achieve a better coverage.

ACPD
5, 2989–3046, 2005

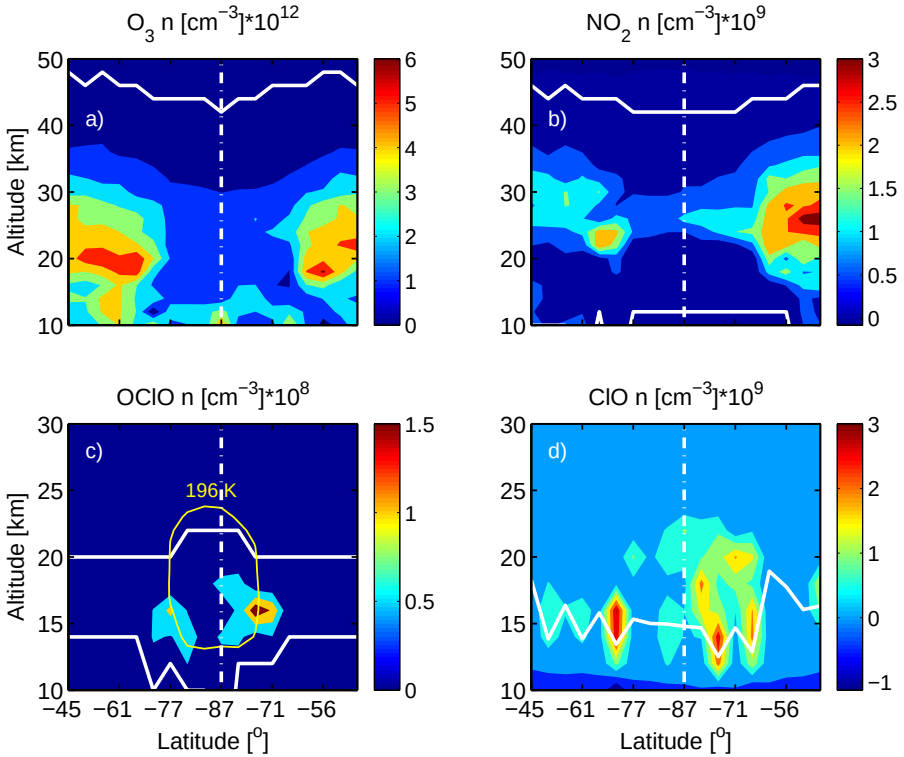

Fig. 13. Retrieved number density profiles of **(a)** OS O_3, **(b)** OS NO_2, **(c)** OS OClO, and **(d)** SMR ClO along the Odin orbit 8565 for latitudes southward of 40° S. The white lines in each plot represent the lowermost and uppermost altitude of significant measurements (i.e., w>0.7). The yellow line in plot (c) represents the isotherm of 196 K (threshold of the PSC formation). The dashed-dotted line in each plot separates the sunrise (left) and sunset (right) measurements.

ACPD
5, 2989–3046, 2005